Computers and Fluids 256 (2023) 105844

Contents lists available at ScienceDirect

Computers and Fluids

journal homepage: www.elsevier.com/locate/compfluid

h-adaptation for high-order discontinuous Galerkin schemes built on local multiwavelet analysis

Javier García Bautista [a,c,*], Marta de la Llave Plata [b], Vincent Couaillier [a], Michel Visonneau [c], Kai Schneider [d]

[a] ONERA-Université Paris-Saclay, DAAA, NFLU, Châtillon, 92320, France
[b] ONERA-Université de Toulouse, DMPE, HEAT, Toulouse, 31055, France
[c] École Centrale de Nantes, CNRS, LHEEA, Nantes, 44321, France
[d] Aix-Marseille Université, CNRS, I2M, Marseille, 13453, France

ARTICLE INFO

Keywords:
High-order methods
h-adaptation
Multiresolution analysis
Multiwavelets

ABSTRACT

We develop and analyze error estimators and mesh adaptation strategies within a discontinuous Galerkin formulation. The basic idea of the study is to reduce the computational cost of the simulation by employing mesh adaptation as a better alternative to the use of uniform grids. The novelty of the study resides in the use of multiwavelets and how their remarkable properties may shed new light on driving the adaptation process. This is motivated by the fact that multiwavelets break any input apart into a hierarchy of low resolution data and subsequently finer details. Our error estimator makes use of multiwavelets' properties while being local to the element, thereby maintaining the parallel efficiency of the solver. Early tests on the one-dimensional viscous Burgers equation have shown convincing results (García Bautista et al. [1]). This work is focused on the laminar backward-facing step configuration to assess the performance of the method in higher dimensions.

1. Introduction

In the framework of the development of the CFD solver *Aghora* [2–4], ONERA is working on the development of *hp*-adaptive high-order discontinuous Galerkin methods (DGMs).

Finite volume methods (FVMs) have been extensively studied and developed by the CFD community [5,6]. FVMs use piecewise constant basis functions defined within the element. On the other hand, finite element methods (FEMs) employ polynomial basis functions of different orders with continuous global support. DGMs appear as a hybrid alternative to the aforementioned methods: the basis functions are local to each element while providing high-order accuracy.

Moreover, DGMs offer the possibility to efficiently adapt the spatial resolution by either modifying the local mesh size (*h*-adaptation), the local polynomial degree (*p*-adaptation), or both simultaneously (*hp*-adaptation). In *h*-adaptation strategies, selected elements are divided into smaller elements (*h*-refinement) or agglomerated into a larger element (*h*-coarsening). On the other hand, *p*-adaptation approaches increase (*p*-enrichment) or lower (*p*-coarsening) the degree p of the polynomial approximation in marked elements. In *hp*-adaptation methods, an *hp*-decision algorithm selects the most appropriate adaptation strategy (*h*- and/or *p*-) to be adopted for each element. Smooth regions in the solution promote *p*-adaptation, whereas regions featuring locally steep gradients (e.g. shocks and boundary layers) are better captured using *h*-adaptation. Overall, the process should maintain at least the same accuracy than the uniformly refined grid (for the same minimum mesh size), yet for a lower number of degrees of freedom (DOFs).

With this in mind, Naddei et al. [7,8] show the benefits of *p*-adaptation, and how its use can considerably reduce the number of DOFs for a given level of accuracy, compared to the use of a uniform approximation order. They compare the performance of different refinement indicators on driving *p*-adaptation under various smooth problems. In a later study, Naddei [9] presents an early assessment of their applicability to *h*-adaptation for smooth flow simulations.

In this work, the focus is on *h*-adaptation strategies, and in particular on the formulation and implementation of *multiwavelet*-based error estimators. Multiwavelets (MWs) belong to the broader field of *multiresolution analysis* (MRA) and they are a generalization of the classical wavelets [10]. The theory of MRA refers to the possibility of representing some given finite energy data as fine-scale contributions and a coarse scale approximation. The aggregation of the coarse scale and the nested sequence of details yields the original data themselves. This scale separation represents the main idea behind wavelets (*scalar* MRA

* Corresponding author at: ONERA-Université Paris-Saclay, DAAA, NFLU, Châtillon, 92320, France.
E-mail addresses: javier.garcia_bautista@onera.fr (J. García Bautista), marta.de_la_llave_plata@onera.fr (M. de la Llave Plata), vincent.couaillier@onera.fr (V. Couaillier), michel.visonneau@ec-nantes.fr (M. Visonneau), kai.schneider@univ-amu.fr (K. Schneider).

https://doi.org/10.1016/j.compfluid.2023.105844
Received 29 October 2021; Received in revised form 8 August 2022; Accepted 27 February 2023
Available online 1 March 2023

theory) and likewise multiwavelets (*vectorial* MRA theory), according to the terminology presented in Strela [11].

In the field of CFD, the natural step forward is for MRA to represent the numerical solution of conservation laws. On a grid it is easy to visualize how more and more details of the conserved quantities can be extracted by refining the mesh until the flow field is fully resolved. These details (also called wavelet coefficients) become negligibly small in regions where the underlying solution is locally smooth. This means that those regions can be captured by using a coarser grid without significant loss of accuracy. On the other hand, regions with large magnitude of wavelet coefficients (such as those presenting steep gradients or discontinuities) may require finer grids. Consequently, the behavior of these coefficients is a suitable measure for adaptivity and allows error control. This idea emerges from the work of Harten [12], who designed a cost-effective FVM flux evaluation based on MRA. However, Harten's original concept did not consider grid adaptation, and was only applied to uniform grids.

A fully adaptive FVM approach based on MRA was later developed in Müller [13,14] by explicitly using biorthogonal wavelets to represent the numerical solution. In his work, Müller applies data compression based on the values of the wavelet coefficients, which in return determine a locally refined grid. Roussel et al. [15],Domingues et al. [16] and Deiterding et al. [17,18] follow another line of research which relies in the recursive use of projection and prediction operators to define the coarse and fine levels of the cell-averaged values of the solution. These are all examples of the use of scalar MRA theory in combination with the FVM to perform mesh adaptation.

The preceding MRA-FVM pairing developed by Müller has been extended to the higher-order DGM framework by Hovhannisyan et al. [19], Gerhard et al. [20,21], and Gerhard and Müller [22]. In this case, the vectorial MRA theory arises as the natural choice. Multiwavelets can be easily combined with the DGM due to their flexibility in matching the order of the approximation while keeping compact support [23]. A similar MRA-DGM which further includes the operators from the partial differential equation as part of the MRA representation was also developed independently by Shelton [24] and Archibald et al. [25]. On a different line of research, the works of Vuik and Ryan [26,27] and Vuik [28] combines the DGM and MWs for the detection of shocks. All these studies employ the so called Alpert's multiwavelets [29,30], in which the MW bases are associated to scaled Legendre polynomials. We will likewise employ this form of MWs in our method, which will be later presented.

As discussed in the previous paragraph, in the MRA-DGM literature the works of Hovhannisyan et al. [19], Gerhard et al. [20,21], and Gerhard and Müller [22] are representative examples of *h*-adaptation based on multiwavelets. Their method intends to improve the efficiency of a prescribed scheme based on a uniform (reference) grid by selecting a refined adapted subgrid on which the calculations are performed, while maintaining the accuracy of the reference solution [23]. The subgrid selection is based on the behavior of the MW coefficients. Namely, a cascade of scales is built from the DG solution on the reference mesh. This representation sheds light on the local structure of the solution. Indeed, the detail coefficients become small with incrementing resolution level when the analyzed solution is smooth. Consequently, thresholding may be used to perform local grid adaptation in those elements in which the MW coefficients still maintain a significant value (refining), and detect the regions where the regularity of the solution allows us to decrease the local resolution while maintaining the desired level of solution accuracy (coarsening). Following this philosophy, we obtain a final mesh that corresponds to a compression of the DG solution.

This method, while soundly based on wavelet theory and accurate [19], bears important constraints. Firstly, a solution on a uniformly refined *reference* grid must be initially foreknown. Gerhard et al. [20] describe how this solution is obtained. Even though the authors specify that no computations have to be performed on the reference grid, they do start from a solution based on that grid. Indeed, this is required so that the adaptive multi-scale structure is defined and the relevant information correctly captured. In the context of unsteady problems, we believe that the authors refer to the fact that the reference solution is used once at the initial time and the adapted subgrid from MRA undertakes the computations for the following time steps. Secondly, only grids which support uniform dyadic subdivisions of the elements are allowed. In this case, the elements are split into sub-elements of equal size and shape. This also includes construction of MWs on triangles as presented by Yu et al. [31]. A possible exception is the *wavelet-free* approach developed by Gerhard [23], which extends the MRA to non-uniform grid hierarchies. However, the work of Gerhard still retains the constraint of using an initial reference grid. Lastly, parallelization may prove challenging due to the pyramidal structure of the MRA technique.

To overcome these shortcomings, in the present work the multiwavelet analysis is performed locally within each element. By being local to the element, adaptation can be applied by starting from a coarse mesh. Besides, more general grids may also be used (not limited by the strict translation and dilation properties of MWs) and the parallel efficiency of the original DGM is conserved.

A requirement of this methodology is however to enrich the original DG element-wise solution, so that the local multiwavelet expansion may extract significant information. This is done by employing a reconstruction process involving the current element and its immediate neighbors. Our approach shares similarities with the higher-order reconstruction scheme developed by Dolejší and Solin [32]. The MRA decomposition is then locally performed on the post-enriched DG solution. The resulting multiwavelet coefficients constitute the backbone of an error estimator which will drive the adaptation process.

Therefore, the main goal of this work is to present a new error estimator grounded on a local MW expansion of a DG solution which is exposed to enrichment by a post-processing reconstruction. The error estimator is first tested for the one-dimensional viscous Burgers equation and then for a two-dimensional laminar flow over the backward-facing step.

This work is organized as follows. In Section 2 the DGM is explained for the general case of the 2-D compressible Navier–Stokes equations. In Section 3 the theoretical background on multiwavelets in 1-D and 2-D is presented. Moreover, the connection between the DGM and MWs is established. Section 4 describes the structure of the h-adaptive DGM based on multiwavelets. We start from the methodology used to enrich the original DG solution and continue with the construction of the local MRA hierarchy. Later, a detailed description of the evaluation of the error estimators, the element marking, and refining strategies are provided. We close this section with the description of the *h*-adaptive algorithm developed in the study. Section 5 presents and discusses the numerical results obtained for the 1-D Burgers equation and the 2-D laminar backward-facing step flow at $Re = 800$ and $Ma = 0.1$. Finally, Section 6 closes the study with conclusions and perspectives for future work.

2. Modal discontinuous Galerkin

In our work the one-dimensional viscous Burgers equation and the two-dimensional compressible Navier–Stokes equations will be considered. This section presents the DGM in the context of the latter, as it is the general case. The particular formulation of the 1-D viscous Burgers equation is described in the Appendix.

Let $\Omega \subset \mathbb{R}^d$ be a bounded domain, where d is the spatial dimension. Given appropriate boundary conditions on $\partial\Omega$ and in the absence of source terms, these equations can be written under the general expression

$$\frac{\partial \mathbf{u}}{\partial t} + \nabla \cdot \left(\boldsymbol{\mathcal{F}}_c(\mathbf{u}) - \boldsymbol{\mathcal{F}}_v(\mathbf{u}, \nabla \mathbf{u}) \right) = 0 , \quad \forall \mathbf{x} \in \Omega, t > 0 , \tag{1}$$

$$\mathbf{u}(\mathbf{x}, 0) = \mathbf{u}_0(\mathbf{x}), \quad \forall \mathbf{x} \in \Omega , \tag{2}$$

where $\mathbf{u}$ is the state vector of conservative variables. The vectors $\mathcal{F}_c$, and $\mathcal{F}_v$ are the convective and viscous fluxes, respectively.

The DGM is based on the discrete weak formulation of the problem given in Eqs. (1)–(2). We now proceed to partition the domain Ω into a shape-regular grid, Ω_h, formed by non-overlapping and non-empty elements K of characteristic size h_K. Interior and boundary faces in Ω_h are defined by $\mathcal{E}_i$ and $\mathcal{E}_b$, respectively, such that $\mathcal{E}_h = \mathcal{E}_i \cup \mathcal{E}_b$. We search for approximate solutions in the function space of piecewise polynomials $\mathcal{V}_h^p = \{\phi \in L^2(\Omega_h) : \ \phi|_K \in \mathcal{P}^p(K), \ \forall K \in \Omega_h\}$ with degree at most p. Let $(\phi_K^1, \dots, \phi_K^{N_p}) \in \mathcal{P}^p(K)$ be a hierarchical and orthonormal modal basis of $\mathcal{V}_h^p$, with dimension $N_p = (p+1)^d$. The element-wise solution is then expressed as

$$\mathbf{u}_h(\mathbf{x}, t) = \sum_{\ell=1}^{N_p} \mathbf{U}_K^\ell(t)\, \phi_K^\ell(\mathbf{x}), \quad \forall \mathbf{x} \in K, K \in \Omega_h, \forall t > 0 \ , \tag{3}$$

where the coefficients $(\mathbf{U}_K^\ell)_{1 \le \ell \le N_p}$ are the degrees of freedom (DOFs) representing the solution in element K. In this work we will consider Cartesian meshes and the basis, $(\phi_K^\ell)_{1 \le \ell \le N_p}$, corresponds to the Legendre polynomials. A mapping is then established between physical and reference space, $\hat{\Omega}_h = [-1, 1]^d$. The variational form of Eq. (1) then follows: find $\mathbf{u}_h$ in $\mathcal{V}_h^p$ such that $\forall\ \phi_h \in \mathcal{V}_h^p$, for each element K, we have

$$\frac{\partial}{\partial t} \int_K \mathbf{u}_h \phi_h \, \mathrm{d}V + \mathcal{L}_c(\mathbf{u}_h, \phi_h) + \mathcal{L}_v(\mathbf{u}_h, \phi_h) = 0 \ . \tag{4}$$

The convective and viscous terms, $\mathcal{L}_c$ and $\mathcal{L}_v$ respectively, will be described in the following sections. To that end, additional notation is required: for a given interface in $\mathcal{E}_i$, we define the average operator $\{\!\{\mathbf{u}\}\!\} = (\mathbf{u}^+ + \mathbf{u}^-)/2$ and the jump operator $[\![\mathbf{u}]\!] = (\mathbf{u}^+ - \mathbf{u}^-) \otimes \mathbf{n}$, where $\mathbf{u}^+$ and $\mathbf{u}^-$ are the traces of $\mathbf{u}$ at the interface between elements K^+ and K^-, and $\mathbf{n}$ represents the outward normal to an element K^+.

2.1. Compressible Navier–Stokes equations

We define $\Omega \subset \mathbb{R}^2$ with $\mathbf{u} = (\rho, \rho\mathbf{v}, \rho E)^T$ the vector of conservative variables. The velocity vector is given by $\mathbf{v} = (v_1, v_2)^T$, and $E = \frac{p}{(\gamma-1)\rho} + \frac{\mathbf{v}\cdot\mathbf{v}}{2}$ represents the specific total energy. The static pressure, p, is defined by the ideal gas law, $p = \rho R T$, and $\gamma = \frac{C_p}{C_v} > 1$ is the ratio of specific heats. The convective and viscous fluxes are then defined by

$$\mathcal{F}_c = \left(\rho, \rho\mathbf{v} \otimes \mathbf{v} + p\bar{\bar{\mathbf{I}}}, (\rho E + p)\mathbf{v}\right)^T , \tag{5}$$

$$\mathcal{F}_v = \left(0, \bar{\bar{\boldsymbol{\tau}}}, \bar{\bar{\boldsymbol{\tau}}} \cdot \mathbf{v} - \mathbf{q}\right)^T , \tag{6}$$

where $\bar{\bar{\boldsymbol{\tau}}} = \mu\left(\nabla\mathbf{v} + (\nabla\mathbf{v})^T - \frac{2}{3}(\nabla\cdot\mathbf{v})\bar{\bar{\mathbf{I}}}\right)$ represents the shear-stress tensor, in which μ is the dynamic viscosity as defined by Sutherland's law. Lastly, the quantity $\mathbf{q} = -k\nabla T$ is the heat-flux vector, with k being the thermal diffusivity.

The discrete variational form of the convective terms in Eq. (4) reads

$$\begin{aligned}\mathcal{L}_c(\mathbf{u}_h, \phi_h) = &\int_K \mathcal{F}_c(\mathbf{u}_h) \cdot \nabla\phi_h \, \mathrm{d}V + \int_{\partial K \cap \mathcal{E}_i} [\![\phi_h]\!]\, \mathbf{h}_c(\mathbf{u}_h^+, \mathbf{u}_h^-, \mathbf{n}) \, \mathrm{d}S \\ &+ \int_{\partial K \cap \mathcal{E}_b} \phi_h^+ \mathcal{F}_c\left(\mathbf{u}_b\right) \cdot \mathbf{n} \, \mathrm{d}S \ ,\end{aligned} \tag{7}$$

where the boundary values $\mathbf{u}_b = \mathbf{u}_b\left(\mathbf{u}_h^+, \mathbf{u}_{\text{ext}}, \mathbf{n}\right)$, with $\mathbf{u}_{\text{ext}}$ a reference external state, are computed so that the boundary conditions are satisfied on $\mathcal{E}_b$. The convective flux on an element face is approximated by the numerical flux $\mathbf{h}_c$ and it must satisfy the conditions of consistency and conservativity [33]. The approximation of the numerical flux is fully defined by the local Lax–Friedrichs flux (LLF), i.e. :

$$\mathbf{h}_c\left(\mathbf{u}_h^+, \mathbf{u}_h^-, \mathbf{n}\right) = \left\{\!\!\left\{ \mathcal{F}_c\left(\mathbf{u}_h\right) \right\}\!\!\right\} \cdot \mathbf{n} + \frac{1}{2}\alpha^{\text{LLF}}\left(\mathbf{u}_h^+ - \mathbf{u}_h^-\right), \tag{8}$$

$$\alpha^{\text{LLF}} = \max\left\{\rho_s(\boldsymbol{\mathcal{J}}(\boldsymbol{u})) : \boldsymbol{u} = \boldsymbol{u}_h^\pm\right\} \ , \tag{9}$$

where $\boldsymbol{\mathcal{J}}(\boldsymbol{u}) = \nabla_{\boldsymbol{u}}\left(\mathcal{F}_c(\boldsymbol{u}) \cdot \boldsymbol{n}\right)$ indicates the Jacobian matrix of the convective fluxes in the direction $\boldsymbol{n}$ and ρ_s its spectral radius.

Finally, for the discrete variational form of the viscous terms, the Bassi–Rebay-2 scheme (BR2) presented by Bassi and Rebay [34] is employed:

$$\begin{aligned}\mathcal{L}_v(\mathbf{u}_h, \phi_h) = &\int_K \mathcal{F}_v(\mathbf{u}_h, \nabla\mathbf{u}_h + \mathbf{L}_h) \cdot \nabla\phi_h \, \mathrm{d}V \\ &- \int_{\partial K \cap \mathcal{E}_i} [\![\phi_h]\!] \left\{\!\!\left\{ \mathcal{F}_v\left(\mathbf{u}_h, \nabla\mathbf{u}_h + \eta_{\text{BR2}}\mathbf{l}_h^e\right) \right\}\!\!\right\} \cdot \mathbf{n} \, \mathrm{d}S \\ &+ \int_{\partial K \cap \mathcal{E}_b} \phi_h^+ \mathcal{F}_v\left(\mathbf{u}_b, \nabla\mathbf{u}_b + \eta_{\text{BR2}}\mathbf{l}_h^e\right) \cdot \mathbf{n} \, \mathrm{d}S \ ,\end{aligned} \tag{10}$$

where the boundary values $\mathbf{u}_b, \nabla\mathbf{u}_b$ are consistent with the boundary conditions imposed on $\mathcal{E}_b$ and η_{BR2} is a user-defined parameter for the stabilization of the method. The local lifting operator, $\mathbf{l}_h^e$, extends its support on the current element K and its neighbors, that is $\text{supp}(\mathbf{l}_h^e) = \{K^+ \cup K^-\}$. It is defined for each internal face $e = \mathcal{E}_{i,K} = \partial K^+ \cap \partial K^-$, as follows:

$$\int_{K^+ \cup K^-} \phi_h \mathbf{l}_h^e \, \mathrm{d}V = -\int_e [\![\phi_h]\!] [\![\mathbf{u}_h]\!] \, \mathrm{d}S \ . \tag{11}$$

An analogous equation consistent with the boundary conditions can be obtained for the boundary faces $\mathcal{E}_b$. The global lifting operator $\mathbf{L}_h$ is defined for the element K as the sum of the local lifting operators, $\mathbf{L}_h = \sum_{e \in \partial K} \mathbf{l}_h^e$.

Lastly, once every term has been defined, Eq. (4) results in a nonlinear system of ordinary differential equations in which the polynomial coefficients, $\mathbf{U}_K^\ell(t)$, are the unknowns to be determined. In this paper the work is focused on steady problems. To evolve the solution in time we use the implicit Euler method. The subsequent linear system of equations is solved by means of the GMRES method with ILU(0) preconditioning [4].

3. Multiwavelets

In this section the basics of multiwavelet theory will be presented. First the concepts will be described in a one-dimensional framework and then we will move to higher spatial dimensions. For further details we refer to the work of Alpert et al. [30] and Strela [11].

3.1. MRA and multiwavelets

Multiresolution analysis allow us to decompose a given input signal into a hierarchy of approximations of that signal at different levels of resolution, as shown by the work of Harten [12]. The level number will be denoted by m, with the highest level of resolution given by $m = \mathcal{M}$. How much detail is captured by a particular resolution level depends on how many subdivisions or elements, N_K, this level owns. Each element $K_{(mj)}$ in a given level m is identified by the index j. If we suppose that the relation between level and number of subdivisions is dyadic (i.e. given a power of two, $N_K = 2^m$) and we work in $L^2(\hat{\Omega}_h)$, with $\hat{\Omega}_h = [-1, 1]$, then the support of the elements is determined by

$$K_{(mj)} = \left[-1 + 2^{-m+1}j, -1 + 2^{-m+1}(j+1)\right] , \tag{12}$$

with $m = 0, \dots, \mathcal{M}$ and $j = 0, \dots, N_K - 1$. Now we define two subspaces connected to each $K_{(mj)}$, denoted by V_m^p, W_m^p. The orthonormal bases for each subspace are called scaling functions, $\mathrm{V}_m^p = \text{span}\left\{\phi_{(mj)}^\ell\right\}$, and multiwavelets, $\mathrm{W}_m^p = \text{span}\left\{\psi_{(mj)}^\ell\right\}$, where $\ell = 1, \dots, N_p$ with $N_p = p + 1$ in the current 1-D context. This is the premise behind Alpert's multiwavelets [29,30]. The following development is based on this family of multiwavelets.

We start from the coarse level $m = 0$ and build up from there. In this case the subspace of scaling functions results in $\mathrm{V}_0^p(\hat{\Omega}_h)$ and its basis are given by [30]. Namely:

$$\phi_{(0,0)}^\ell(\xi) = \phi^\ell(\xi) = \begin{cases} \sqrt{\frac{2(\ell-1)+1}{2}}\, P^\ell(\xi), & \xi \in \hat{\Omega}_h \\ 0, & \text{otherwise} \end{cases} \tag{13}$$

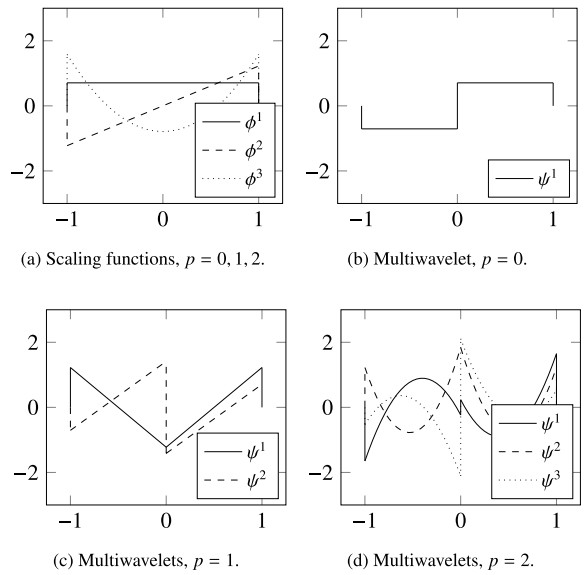

(a) Scaling functions, $p = 0, 1, 2$. (b) Multiwavelet, $p = 0$.

(c) Multiwavelets, $p = 1$. (d) Multiwavelets, $p = 2$.

Fig. 1. Scaling functions and multiwavelets.

where $P^{\ell}(\xi)$ indicates the Legendre polynomial of degree $\ell - 1$. Scaling functions in Eq. (13) up to $p = 2$ are plotted in Fig. 1(a). On the other hand, multiwavelets undergo a more complex building process. The algorithm starts with a piecewise monomial of degree $(\ell - 1)$ defined in $\hat{\Omega}_h = [-1, 1]$. A Gram–Schmidt orthonormalization is followed by an operation to increase the number of vanishing moments of the resulting function. This is enforced by ensuring orthogonality with respect to a higher degree monomial. The complete algorithm can be found in [29]. The multiwavelets that span the subspace $\mathrm{W}_0^p(\hat{\Omega}_h)$ are thus formed by these orthonormal functions $f^{(\ell,p)}(x)$ as follows:

$$\psi^{\ell}_{(0,0)}(\xi) = \psi^{\ell}(\xi) = \begin{cases} (-1)^{(\ell-1)+p+1} f^{(\ell,p)}(-\xi), & \xi \in [-1, 0] \\ f^{(\ell,p)}(\xi), & \xi \in [0, 1] \\ 0, & \text{otherwise} \end{cases} \tag{14}$$

Multiwavelets in Eq. (14) with $p = 0, 1, 2$ are plotted in Fig. 1(b) to 1(d), respectively. At this point, the basis of $\mathrm{V}_0^p, \mathrm{W}_0^p$ have been defined. To describe successive subspaces for $m > 0$ we require the mapping $\xi \mapsto \frac{2(x-x_c)}{h_K}$, with $x \in K_{(m,j)}$. Also, x_c and h_K represent the center and the size of element $K_{(m,j)}$, respectively. The basis $\phi^{\ell}_{(m,j)}, \psi^{\ell}_{(m,j)} \in \mathrm{V}_m^p, \mathrm{W}_m^p$ are generated by dilation and translation of $\phi^{\ell}_{(0,0)}, \psi^{\ell}_{(0,0)} \in \mathrm{V}_0^p, \mathrm{W}_0^p$, namely,

$$\phi^{\ell}_{(m,j)}(x) = \sqrt{\frac{2}{h_K}}\, \phi^{\ell}\left(\frac{2(x - x_c)}{h_K}\right), \qquad \ell = 1, \dots, N_p, \tag{15}$$

$$\psi^{\ell}_{(m,j)}(x) = \sqrt{\frac{2}{h_K}}\, \psi^{\ell}\left(\frac{2(x - x_c)}{h_K}\right), \qquad j = 0, \dots, N_K - 1, \tag{16}$$

with $m = 0, \dots, \mathcal{M}$. Both scaling functions and multiwavelets support extends to the current element defined by $K_{(m,j)}$. That is $\mathrm{supp}\left(\phi^{\ell}_{(m,j)}\right) = \mathrm{supp}\left(\psi^{\ell}_{(m,j)}\right) = K_{(m,j)}$. Moreover, they are L^2-normalized, $\left\|\phi^{\ell}_{(m,j)}\right\|_{L^2} = \left\|\psi^{\ell}_{(m,j)}\right\|_{L^2} = 1$, and share the following orthonormality relations:

$$\left\langle \phi^{\ell}_{(m,j)}, \phi^{\ell'}_{(m,j')} \right\rangle_{K_{(m,j)}} = \delta_{\ell,\ell'}\, \delta_{j,j'}, \tag{17a}$$

$$\left\langle \phi^{\ell}_{(m,j)}, \psi^{\ell'}_{(m,j')} \right\rangle_{K_{(m,j)}} = 0, \tag{17b}$$

$$\left\langle \psi^{\ell}_{(m,j)}, \psi^{\ell'}_{(m',j')} \right\rangle_{K_{(m,j)}} = \delta_{\ell,\ell'}\, \delta_{j,j'}\, \delta_{m,m'}, \tag{17c}$$

with $\langle\ \rangle$ representing the inner product. Additionally, inherited by Alpert's algorithm, multiwavelets have $M = \ell + p$ vanishing moments, which means that the multiwavelets are orthogonal to polynomials of degree M. Therefore,

$$\left\langle P, \psi^{\ell}_{(m,j)} \right\rangle_{K_{(m,j)}} = 0, \qquad \forall P \in \mathcal{P}^M\left(K_{(m,j)}\right). \tag{18}$$

Further details can be found in [19]. A strong relation exists between the subspaces defined in the MRA. The multiwavelet subspace W_m^p is the orthogonal complement of the scaling function space V_m^p in V_{m+1}^p [30], namely,

$$\mathrm{V}_{m+1}^p = \mathrm{V}_m^p \oplus \mathrm{W}_m^p; \quad \mathrm{W}_m^p \perp \mathrm{V}_m^p\ . \tag{19}$$

By successive application of Eq. (19), a hierarchy of multiwavelet subspaces can be derived:

$$\mathrm{V}_m^p = \mathrm{V}_0^p \oplus \mathrm{W}_0^p \oplus \mathrm{W}_1^p \oplus \cdots \oplus \mathrm{W}_{m-1}^p\ . \tag{20}$$

3.2. Coupling of DGM and multiwavelets

If we remember the DGM described in Section 2, the basis employed for the element-wise solution are built upon Legendre polynomials. As mentioned above, the same occurs with the basis of the scaling function subspace in the multiwavelet formulation. Therefore a direct relation can be established between both approaches. We consider a dyadic mesh composed of $N_K = 2^{\mathcal{M}}$ elements and $\Omega_h = \hat{\Omega}_h$, so that the multiwavelet formulation holds. By extending the approximate DG solution in element $K = K_{(\mathcal{M},j)}$ in Eq. (3) over the entire domain Ω_h, we have:

$$\begin{aligned} u_h(x,t) &= \sum_K \sum_{\ell=1}^{N_p} U_K^{\ell}(t)\, \phi_K^{\ell}(x), \qquad \forall x \in K_{(\mathcal{M},j)},\ K_{(\mathcal{M},j)} \in \Omega_h. \\ &= \sum_{j=0}^{N_K-1} \sum_{\ell=1}^{N_p} U^{\ell}_{(\mathcal{M},j)}(t)\, \phi^{\ell}_{(\mathcal{M},j)}(x) \\ &= \sum_{j=0}^{N_K-1} \sum_{\ell=1}^{N_p} U^{\ell}_{(\mathcal{M},j)}(t)\, \phi^{\ell}_{(0,0)}\left(\frac{2(x - x_c)}{h_K}\right). \end{aligned} \tag{21}$$

We can now express the approximate solution in terms of the single-scale decomposition on level $\mathcal{M}$ [20], which is a combination of the scaling functions defined in Eq. (15). Namely,

$$\begin{aligned} u_h(x,t) &= \sum_{j=0}^{N_K-1} \sum_{\ell=1}^{N_p} s^{\ell}_{(\mathcal{M},j)}(t)\, \phi^{\ell}_{(\mathcal{M},j)}(x) \\ &= \sqrt{\frac{2}{h_K}} \sum_{j=0}^{N_K-1} \sum_{\ell=1}^{N_p} s^{\ell}_{(\mathcal{M},j)}(t)\, \phi^{\ell}_{(0,0)}\left(\frac{2(x - x_c)}{h_K}\right), \end{aligned} \tag{22}$$

with $h_K = 2^{-\mathcal{M}+1}$. The single-scale decomposition differs from the DG representation only by a scaling term. Hence, by comparing Eq. (21) to (22), the relation between the DG coefficients and the single-scale coefficients is given by

$$s^{\ell}_{(\mathcal{M},j)}(t) = 2^{-\mathcal{M}/2} U^{\ell}_{(\mathcal{M},j)}(t). \tag{23}$$

By using Eq. (20), a scaling function subspace can be hierarchically divided into a cascade of multiwavelet subspaces plus a baseline scaling function subspace corresponding to the lowest resolution level. If we apply this to Eq. (22), we obtain the multiscale decomposition of the approximate solution. Namely:

$$u_h = \sum_{\ell=1}^{N_p} \left(s^{\ell}_{(0,0)}\, \phi^{\ell}_{(0,0)} + \sum_{m=0}^{\mathcal{M}-1} \sum_{j=0}^{N_K-1} d^{\ell}_{(m,j)}\, \psi^{\ell}_{(m,j)} \right), \tag{24}$$

where

$$s^{\ell}_{(0,0)} = \left\langle u_h, \phi^{\ell}_{(0,0)} \right\rangle_{K_{(0,0)}}, \tag{25a}$$

$$d^{\ell}_{(m,j)} = \left\langle u_h, \psi^{\ell}_{(m,j)} \right\rangle_{K_{(m,j)}}, \tag{25b}$$

are the scaling function and multiwavelet coefficients, respectively. These coefficients can be computed efficiently using the so-called

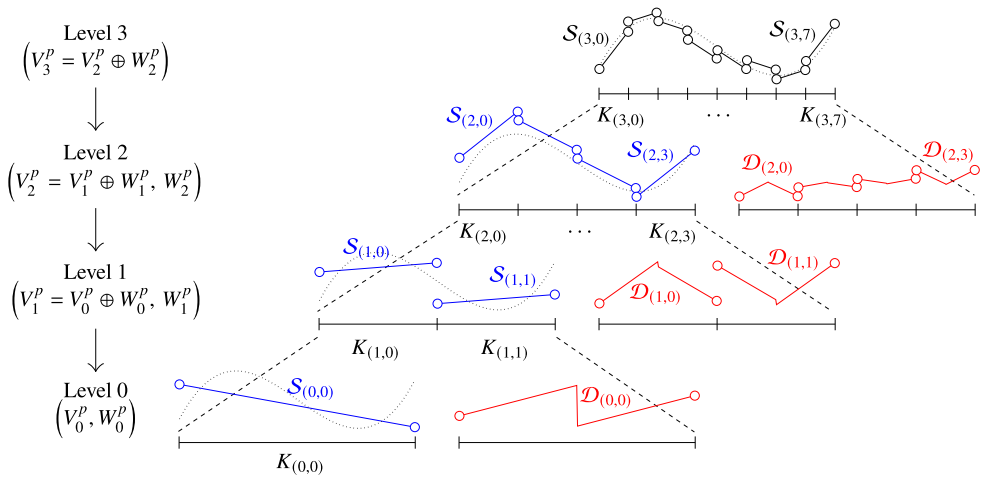

Fig. 2. Four-level multiscale representation by multiwavelets of second order DG solution. We use the nomenclature $\mathcal{S}_{(mj)} = \sum_\ell s^\ell_{(mj)} \phi^\ell_{(mj)}$ (single-scale) and $\mathcal{D}_{(mj)} = \sum_\ell d^\ell_{(mj)} \psi^\ell_{(mj)}$ (multiscale). The highest resolution level is $\mathcal{M} = 3$ and $\Omega_h = \bigcup_j K_{(\mathcal{M}j)}$.

quadrature mirror filter (QMF) coefficients, $H^{(0)}_{\ell k}, H^{(1)}_{\ell k}, G^{(0)}_{\ell k}, G^{(1)}_{\ell k}$, as described by Geronimo et al. [35]. The relations between the coefficients on two consecutive levels are given by:

$$s^\ell_{(m-1,j)} = \sum_{k=1}^{N_p} \left(H^{(0)}_{\ell k} s^k_{(m2j)} + H^{(1)}_{\ell k} s^k_{(m2j+1)} \right), \quad \ell = 1, \dots, N_p, \tag{26a}$$

$$d^\ell_{(m-1,j)} = \sum_{k=1}^{N_p} \left(G^{(0)}_{\ell k} s^k_{(m2j)} + G^{(1)}_{\ell k} s^k_{(m2j+1)} \right), \quad m = 1, \dots, \mathcal{M} \tag{26b}$$

with $j = 0, \dots, 2^{(m-1)} - 1$. Coarser scales of the solution can be obtained by the successive application of Eq. (26a). Furthermore, the multiwavelet coefficients between scales are given by Eq. (26b). Fig. 2 shows the multiscale representation for a second order DG solution. Effectively, the multiscale decomposition divides the single-scale coefficients $s^\ell_{(\mathcal{M}j)}$ into a smaller group of coefficients $s^\ell_{(0,0)}$ and $(\mathcal{M}-1)$ blocks of multiwavelet or detail coefficients $d^\ell_{(mj)}$. The former is a coarse approximation of the original solution and the latter carries the information between scales. This multiscale information represent the individual characteristics of the solution in a hierarchy of ascending resolution.

3.3. Two-dimensional multiwavelets

In the 2-D case the domain in which the scaling functions and multiwavelets operate is $\Omega = [-1, 1]^2$ which is discretized into an equal number of $N_K = 2^m$ elements along each of the x- and y-direction, resulting in a total of N_K^2 elements per level m. The 1-D development of the previous section can be extended to higher dimensions in a straightforward manner by using tensor products of the basis. We use the nomenclature $N_p^{1D} = p+1$ and $N_p^{2D} = (p+1)^2$. Therefore, the tensor product results in

$$\boldsymbol{\Phi}^\ell_{(mj)}(\mathbf{x}) = \phi^{\ell_x}_{(m,j_x)}(x)\, \phi^{\ell_y}_{(m,j_y)}(y), \quad m = 0, \dots, \mathcal{M}, \tag{27a}$$

$$\boldsymbol{\Psi}^{\ell,\alpha}_{(mj)}(\mathbf{x}) = \psi^{\ell_x}_{(m,j_x)}(x)\, \phi^{\ell_y}_{(m,j_y)}(y), \quad \ell = N_p^{1D}(\ell_x - 1) + \ell_y, \tag{27b}$$

$$\boldsymbol{\Psi}^{\ell,\beta}_{(mj)}(\mathbf{x}) = \phi^{\ell_x}_{(m,j_x)}(x)\, \psi^{\ell_y}_{(m,j_y)}(y), \quad j = N_K j_x + j_y, \tag{27c}$$

$$\boldsymbol{\Psi}^{\ell,\gamma}_{(mj)}(\mathbf{x}) = \psi^{\ell_x}_{(m,j_x)}(x)\, \psi^{\ell_y}_{(m,j_y)}(y), \tag{27d}$$

with $\ell_x, \ell_y = 1, \dots, N_p^{1D}$ and $j_x, j_y = 0, \dots, N_K - 1$. The expression $\boldsymbol{\Phi}^\ell_{(mj)}$ constitutes the basis of the scaling function subspace, given by $\mathbf{V}_m^p = \text{span}\{\boldsymbol{\Phi}^\ell_{(mj)}\}$; and $\boldsymbol{\Psi}^\ell_{(mj)}$ represents the basis of the multiwavelet subspace. The superscripts α, β and γ denote the x-, y-, and xy-directions, respectively. Namely:

$$\mathbf{W}_m^{p,\alpha} = \text{span}\{\boldsymbol{\Psi}^{\ell,\alpha}_{(mj)}\}, \tag{28a}$$

$$\mathbf{W}_m^{p,\beta} = \text{span}\{\boldsymbol{\Psi}^{\ell,\beta}_{(mj)}\}, \tag{28b}$$

$$\mathbf{W}_m^{p,\gamma} = \text{span}\{\boldsymbol{\Psi}^{\ell,\gamma}_{(mj)}\}. \tag{28c}$$

Further details can be found in the work of Vuik and Ryan [26]. The relation between the DG coefficients and the single-scale coefficients is equivalent to Eq. (23) from the previous section, and is now given by

$$\mathbf{s}^\ell_{(\mathcal{M}j)} = 2^{-\mathcal{M}} \mathbf{U}^\ell_{(\mathcal{M}j)}. \tag{29}$$

Applying the QMF coefficients presented in Geronimo et al. [35] the lower-lever single-scale and multiwavelet coefficients for each component can be calculated efficiently as follows:

$$\mathbf{s}^\ell_{(m-1,j)} = \sum_{\bar{j}_x,\bar{j}_y=0}^{1} \sum_{k_x,k_y=1}^{N_p^{1D}} \left[H^{(\bar{j}_x)}_{\ell_x,k_x}\, H^{(\bar{j}_y)}_{\ell_y,k_y}\, \mathbf{s}^k_{(m,2j+\bar{j})} \right], \tag{30a}$$

$$\mathbf{d}^{\ell,\alpha}_{(m-1,j)} = \sum_{\bar{j}_x,\bar{j}_y=0}^{1} \sum_{k_x,k_y=1}^{N_p^{1D}} \left[G^{(\bar{j}_x)}_{\ell_x,k_x}\, H^{(\bar{j}_y)}_{\ell_y,k_y}\, \mathbf{s}^k_{(m,2j+\bar{j})} \right], \tag{30b}$$

$$\mathbf{d}^{\ell,\beta}_{(m-1,j)} = \sum_{\bar{j}_x,\bar{j}_y=0}^{1} \sum_{k_x,k_y=1}^{N_p^{1D}} \left[H^{(\bar{j}_x)}_{\ell_x,k_x}\, G^{(\bar{j}_y)}_{\ell_y,k_y}\, \mathbf{s}^k_{(m,2j+\bar{j})} \right], \tag{30c}$$

$$\mathbf{d}^{\ell,\gamma}_{(m-1,j)} = \sum_{\bar{j}_x,\bar{j}_y=0}^{1} \sum_{k_x,k_y=1}^{N_p^{1D}} \left[G^{(\bar{j}_x)}_{\ell_x,k_x}\, G^{(\bar{j}_y)}_{\ell_y,k_y}\, \mathbf{s}^k_{(m,2j+\bar{j})} \right], \tag{30d}$$

where

$$m = 1, \dots, \mathcal{M},$$
$$\bar{j} = \bar{j}_x + \bar{j}_y, \qquad k = N_p^{1D}(k_x - 1) + k_y,$$
$$j = N'_K j_x + j_y, \qquad j_x, j_y = 0, \dots, N'_K - 1,$$

with $N'_K = 2^{(m-1)}$. The index $\bar{j}$ accounts for the fact that one coefficient at level $m-1$ results from the contribution of four coefficients at level m. Finally, the multiscale decomposition presented in Eq. (24) can be expressed as:

$$\mathbf{u}_h = \sum_{\ell=1}^{N_p^{2D}} \mathbf{s}^\ell_{(0,0)}\, \boldsymbol{\Phi}^\ell_{(0,0)} + \sum_{\ell=1}^{N_p^{2D}} \sum_{m=0}^{\mathcal{M}-1} \sum_{j=0}^{N_K^2} \left[\mathbf{d}^{\ell,\alpha}_{(mj)}\, \boldsymbol{\Psi}^{\ell,\alpha}_{(mj)} + \mathbf{d}^{\ell,\beta}_{(mj)}\, \boldsymbol{\Psi}^{\ell,\beta}_{(mj)} + \mathbf{d}^{\ell,\gamma}_{(mj)}\, \boldsymbol{\Psi}^{\ell,\gamma}_{(mj)} \right]. \tag{31}$$

4. *h*-adaptive DGM based on multiwavelets

In the introduction to this work (Section 1), we have presented the historical evolution of the *multiresolution-based grid adaptation* in CFD.

In particular, we have highlighted the relevance of multiwavelets in combination with the discontinuous Galerkin method (e.g., see Hovhannisyan et al. [19] or Gerhard et al. [20]). This approach is accurate and solidly built on wavelet theory Gerhard and Müller [22]. However, we have also observed that it is subjected to a series of limitations. These range from the requirement of an initial reference solution through the restriction to nested dyadic grids to the challenge in parallelizing the multiresolution analysis.

As opposed to the approach discussed above, in this research we aim at developing a mesh adaptation algorithm that starts from a coarse solution and proceed with the refinement where required, with no initial reference grid involved. Traditionally, to deal with this problem, *a posteriori* error estimators have been used to drive the adaptation, which are computed from the discrete solution and try to measure the error of the adaptive solution. Examples of these indicators can be found in the work of Mavriplis [36], Mitchell and McClain [37], Bey and Tinsley Oden [38], and Adjerid et al. [39].

Here we propose a method which locally confines the MRA decomposition to the element. More specifically, an independent multiwavelet decomposition is performed locally for every element of the physical domain. We call our approach *local multiresolution*. This is a departure from the preceding work of Hovhannisyan et al. [19] and Gerhard and Müller [22], in which the MRA decomposition encompasses the entire domain. Their approach can be classified as *global multiresolution*.

Fig. 3 shows the two approaches. The global MRA, Fig. 3(a), produces multiple levels of information thanks to the highly detailed approximate solution at level $\mathcal{M}$. On the other hand, the local MRA, Fig. 3(b), do not require such a solution. Instead, our target is to sufficiently resemble its behavior by providing extra information (*enriching*). To achieve this, we manufacture a more accurate approximation for each element K separately. Then a subsequent MRA is applied locally, producing a two-level multiscale representation within the element. In particular, we are interested in the multiwavelet part of the multiscale representation. Indeed, multiwavelet coefficients can be interpreted as messengers of individual features of the approximation. Thanks to this property multiwavelets become an excellent candidate to measure the discretization error. In turn, the estimation provided by the multiwavelets can be used later to drive adaptation.

In the following sections we describe in detail each of the aforementioned steps, starting with the procedure to manufacture a new approximation from the existing DG solution.

4.1. Reconstruction of new enriched approximation from DG solution

We intend to reach an analogue to the highly detailed approximate solution u_h^* from which Hovhannisyan et al. [19] and Gerhard and Müller [22] start their global MRA, as illustrated in Fig. 3(a). The idea being that we can use later that analogue as a launchpad to start our local MRA, as represented in Fig. 3(b).

To build the analogue we turn to the work of Dolejší and Solin [32]. In their research, the authors assemble a higher-order reconstruction $\tilde{u}_h$ which they later measure against the original solution u_h to guide the *hp*-adaptation process. By observing that the discretization error, $e_h = u - u_h$, and its approximation by the higher-order reconstruction, $\mathcal{E}_h = \tilde{u}_h - u_h$, have similar element-wise distribution, $e_h \approx \mathcal{E}_h$, they verify numerically that the reconstruction approximates better the exact solution than the original. Inspired by this idea, we build a more accurate approximation $\tilde{u}_h$ by considering the contribution of the current element K and its neighbors. This procedure will be presented first in the 1-D setup. The extension to higher dimensions will be described later.

We define the support of $\tilde{u}_h$ according to the two-level multiscale representation of element K, as shown in Fig. 3(b). In this context, we have

$$\operatorname{supp}\left(\tilde{u}_h\right) = \bigcup_{i=0}^{N_{\text{art}}-1} \kappa_i, \qquad \text{with } N_{\text{art}} = 2, \tag{32}$$

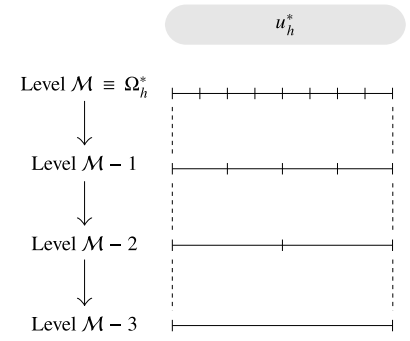

(a) Global multiresolution [19].

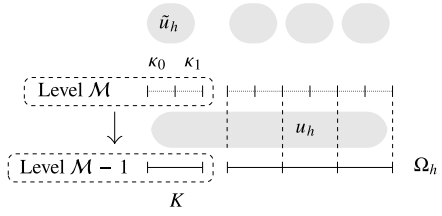

(b) Local multiresolution.

Fig. 3. Different multiscale representations.

where the *artificial* sub-elements κ_i would originate from the twofold isotropic subdivision of element K. The new approximation $\tilde{u}_h$ is then described by N_{art} piecewise polynomial functions. Namely:

$$\tilde{u}_h = \sum_i \tilde{u}_{h,i}, \qquad \tilde{u}_{h,i} \in \mathcal{P}^p(\kappa_i), \quad i = 0, \dots, N_{\text{art}} - 1. \tag{33}$$

Note that the term *artificial* is employed to indicate κ_i despite the fact that no actual mesh subdivision actually occurs at this stage. In fact, our implementation associates $\tilde{u}_h$ to the element K. However we believe that the definition of κ_i may help the reader to better understand the procedure.

In order to assemble $\tilde{u}_h$ we propose three different approaches depending on how data from neighboring elements are accounted for:

1. *κ-reconstruction*: $\tilde{u}_h$ is built from the immediate neighbors of sub-elements κ_i.
2. *K-reconstruction*: $\tilde{u}_h$ is constructed from the immediate neighbors of element K.
3. *Γ-reconstruction*: $\tilde{u}_h$ is set up from the solution jumps at the faces of sub-elements κ_i.

Fig. 4 illustrates the different methods. The following Sections 4.1.1 to 4.1.3 will describe them in detail.

4.1.1. κ-Reconstruction

The construction of $\tilde{u}_h$ is performed by a *least-square function approximation* from the block $\mathcal{A}_i$, defined as follows:

$$\mathcal{A}_i = \kappa_{1-i}^{(K+i-1)} \cup \kappa_i^{(K)} \cup \kappa_{1-i}^{(K+i)}, \qquad i = 0, \dots, N_{\text{art}} - 1, \tag{34}$$

where $N_{\text{art}} = 2$ and the superscript indicates from which $K \in \Omega_h$ the artificial sub-element κ originates. Then we define the polynomial function $\tilde{U}_{h,i} \in \mathcal{P}^p(\mathcal{A}_i)$ by

$$\tilde{U}_{h,i}(x,t) = \sum_{\ell=1}^{N_p} \tilde{X}_{\mathcal{A}_i}^{\ell}(t)\, \phi_{\mathcal{A}_i}^{\ell}(x), \qquad \forall x \in \mathcal{A}_i. \tag{35}$$

where $\tilde{X}_{\mathcal{A}_i}^{\ell}$ are the unknown coefficients. They are calculated by minimizing the error in the least-square sense with respect to the original

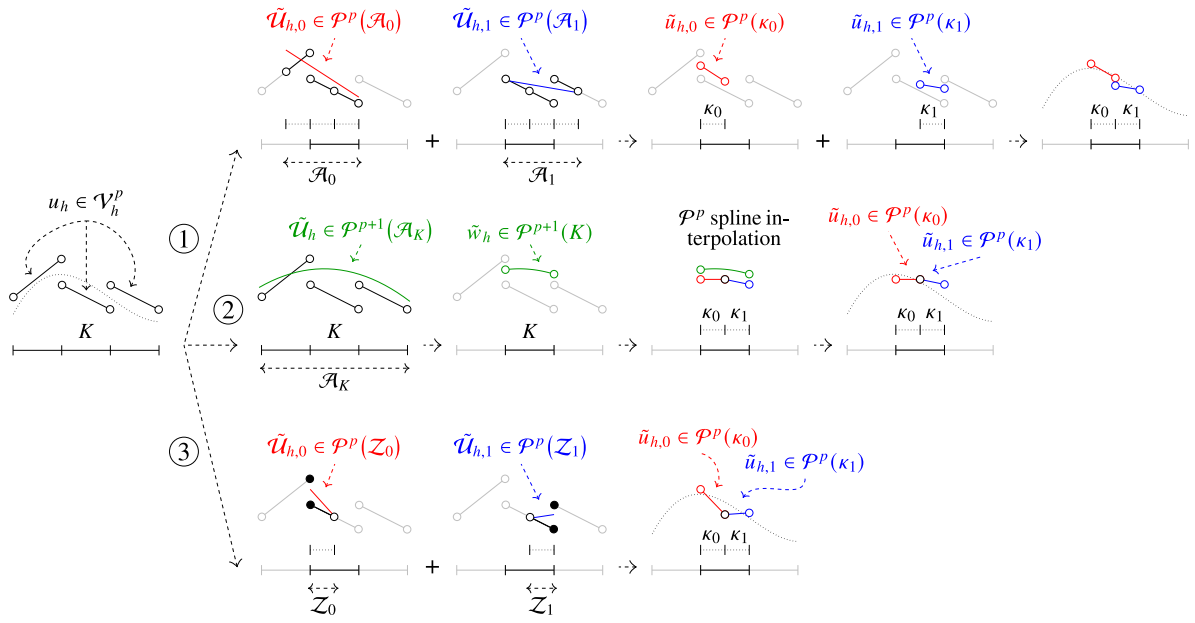

Fig. 4. Reconstruction procedures developed in this work. From top to bottom: ① *κ-reconstruction*, ② *K-reconstruction*, and ③ *Γ-reconstruction*.

approximation u_h. Namely:

$$\tilde{X}^{\ell}_{\mathcal{A}_i} = \arg\min \left\| u_h - \tilde{\mathcal{U}}_{h,i} \right\|^2_{L^2(\mathcal{A}_i)}. \tag{36}$$

Solving the optimization problem in Eq. (36), we obtain the linear algebraic system

$$A_{k,\ell}\, \tilde{X}^{\ell}_{\mathcal{A}_i} = b^k, \tag{37}$$

where:

$$A_{k,\ell} = \sum_{\kappa \in \mathcal{A}_i} \left\langle \phi^k_\kappa, \phi^\ell_\kappa \right\rangle_\kappa, \tag{38a}$$

$$b^k = \sum_{\kappa \in \mathcal{A}_i} \left\langle \phi^k_\kappa, u_h \right\rangle_\kappa, \qquad k, \ell = 1, \dots, N_p\ . \tag{38b}$$

Now the polynomial function $\tilde{\mathcal{U}}_{h,i}$ is fully characterized within the block $\mathcal{A}_i$. Lastly, we restrict $\tilde{\mathcal{U}}_{h,i}$ just to sub-element $\kappa_i^{(K)}$ and arrive to the piecewise polynomial function $\tilde{u}_{h,i}$. Namely:

$$\tilde{u}_{h,i} = \tilde{\mathcal{U}}_{h,i}\Big|_{\kappa_i^{(K)}}, \qquad i = 0, \dots, N_{\text{art}} - 1. \tag{39}$$

4.1.2. K-Reconstruction

The first steps in the assembly of $\tilde{u}_h$ follow the same instructions described by Dolejší and Solin [32]. That is, we build a high-order polynomial reconstruction by a *least-square function approximation* from a block $\mathcal{A}_K$ defined as follows:

$$\mathcal{A}_K = K \cup \left\{ K' \in \Omega_h \mid K' \text{ share at least a face with } K \right\}. \tag{40}$$

We then establish the higher-order polynomial $\tilde{\mathcal{U}}_h \in \mathcal{P}^{p+1}(\mathcal{A}_K)$ by

$$\tilde{\mathcal{U}}_h(x,t) = \sum_{\ell=1}^{N'_p} \tilde{X}^{\ell}_{\mathcal{A}_K}(t)\, \phi^{\ell}_{\mathcal{A}_K}(x), \qquad \forall x \in \mathcal{A}_K\,, \tag{41}$$

with $N'_p = (p+2)$. Their unknown coefficients $\tilde{X}^{\ell}_{\mathcal{A}_K}$ are determined by solving the optimization problem presented in Eq. (36) and the following linear system on the new block $\mathcal{A}_K$. It is worth mentioning that the optimization problem is solved by using the L^2-norm, whereas Dolejší and Solin [32] employ the H^1-norm. We have tested both norms and found very little difference in the final reconstruction. This justifies the use of the simpler L^2-norm in our work. Next we define the higher-order piecewise polynomial $\tilde{w}_h \in \mathcal{P}^{p+1}(K)$ as the restriction of $\tilde{\mathcal{U}}_h$ on K. Namely:

$$\tilde{w}_h = \tilde{\mathcal{U}}_h\Big|_K. \tag{42}$$

Once the higher-order approximation $\tilde{w}_h$ is restricted to K, we move to set up $\tilde{u}_h$ by using the information provided by this new approximation. If we recall the definition of $\tilde{u}_h$, that is, Eq. (33):

$$\tilde{u}_h = \sum_i \tilde{u}_{h,i} = \sum_i \sum_{\ell=1}^{N_p} \tilde{U}^{\ell}_{\kappa_i}\, \phi^{\ell}_{\kappa_i}, \qquad i = 0, \dots, N_{\text{art}} - 1. \tag{43}$$

In order to build $\tilde{u}_h$ we use a p-degree *spline interpolation* on the artificial sub-elements κ_i. Therefore, we have $N_{\text{art}} N_p$ unknown coefficients $\tilde{U}^{\ell}_{\kappa_i}$ to evaluate. The same numbers of conditions are required to evaluate the unknowns. We meet the conditions by projecting $\tilde{w}_h$ on a set of N_p *Gauss–Lobatto* integration points for each κ_i. Thus reaching $N_{\text{art}} N_p$ conditions for the same number of unknowns. This results on a linear system that solves for $\tilde{U}^{\ell}_{\kappa_i}$.

4.1.3. Γ-Reconstruction

In the final method, $\tilde{u}_h$ is built from a simpler *least-square function approximation* from the block $\mathcal{Z}_i$. The block is defined as

$$\mathcal{Z}_i = \kappa_i^{(K)} \cup \Gamma_i, \qquad \Gamma_i = \left\{ \partial\kappa_{1-i}^{(K-1+2i)} \cap \partial\kappa_i^{(K)} \right\}, \tag{44}$$

with $i = 0, \dots, N_{\text{art}} - 1$. The block $\mathcal{Z}_i$ is simply κ_i plus the shared face of the nearest neighboring element, denoted by Γ_i. This means that this method integrates the solution jump between element K and their neighbors $K-1$ and $K+1$ into $\tilde{u}_h$. Similarly to the two earlier methods, we define the polynomial function $\tilde{\mathcal{U}}_{h,i} \in \mathcal{P}^p(\mathcal{Z}_i)$ by

$$\tilde{\mathcal{U}}_{h,i}(x,t) = \sum_{\ell=1}^{N_p} \tilde{X}^{\ell}_{\mathcal{Z}_i}(t)\, \phi^{\ell}_{\mathcal{Z}_i}(x), \qquad \forall x \in \mathcal{Z}_i, \tag{45}$$

where the coefficients $\tilde{X}^{\ell}_{\mathcal{Z}_i}$ are calculated by solving Eq. (36) on the new block $\mathcal{Z}_i$. The resulting linear system can be expressed as

$$A_{k,\ell}\, \tilde{X}^{\ell}_{\mathcal{Z}_i} = b^k, \tag{46}$$

where

$$A_{k,\ell} = \left[\phi^k \phi^\ell\right]_{\Gamma_i} + \left\langle \phi^k_{\kappa_i}, \phi^\ell_{\kappa_i} \right\rangle_{\kappa_i}, \tag{47a}$$

$$b^k = \left[\phi^k u_h\right]_{\Gamma_i} + \left\langle \phi^k_{\kappa_i}, u_h \right\rangle_{\kappa_i}, \qquad k, \ell = 1, \dots, N_p\ . \tag{47b}$$

Finally, we define $\tilde{u}_{h,i}$ by restricting $\tilde{\mathcal{U}}_{h,i}$ just to sub-element $\kappa_i^{(K)}$, in the same way as Eq. (39).

4.1.4. Two-dimensional reconstruction

In the case of a 2-D reconstruction we define the support of the new enriched approximation $\tilde{\mathbf{u}}_h$ as follows:

$$\text{supp}\left(\tilde{\mathbf{u}}_h\right) = \bigcup_{i=0}^{N_{\text{art}}-1} \kappa_i, \quad \text{with } N_{\text{art}} = 4, \tag{48}$$

where κ_i represent the artificial sub-elements from the fourfold isotropic subdivision of element K. The term *artificial* retains the same meaning as described in the 1-D reconstruction. Similarly, $\tilde{\mathbf{u}}_h$ is composed of N_{art} piecewise polynomial functions. That is:

$$\tilde{\mathbf{u}}_h = \sum_i \tilde{\mathbf{u}}_{h,i}, \qquad \tilde{\mathbf{u}}_{h,i} \in \mathcal{P}^p(\kappa_i), \quad i = 0, \dots, N_{\text{art}} - 1. \tag{49}$$

Of the three reconstructions approaches proposed in the previous 1-D setting, only the *κ–reconstruction* method (see Section 4.1.1) will extended to the 2-D context. If we recall this method, the new approximation $\tilde{\mathbf{u}}_h$ is set up by considering the immediate neighbors of sub-elements κ_i. This is performed by a *least-square function approximation* applied to the block $\mathcal{A}_i$, which is characterized by

$$\mathcal{A}_i = \bigcup_{e \in \partial\kappa_i} \left\{\kappa^+ \cup \kappa^-\right\}^e, \qquad i = 0, \dots, N_{\text{art}} - 1, \tag{50}$$

where $e \in \partial\kappa_i$ represent the individual faces of κ_i. The next step is to define the polynomial function $\tilde{\boldsymbol{\mathcal{U}}}_{h,i} \in \mathcal{P}^p\left(\mathcal{A}_i\right)$ by

$$\tilde{\boldsymbol{\mathcal{U}}}_{h,i}(\mathbf{x}, t) = \sum_{\ell=1}^{N_p} \tilde{\mathbf{X}}_{\mathcal{A}_i}^{\ell}(t)\, \phi_{\mathcal{A}_i}^{\ell}(\mathbf{x}), \quad \forall \mathbf{x} \in \mathcal{A}_i, \tag{51}$$

where $\tilde{\mathbf{X}}_{\mathcal{A}_i}^{\ell}$ are the coefficients to be calculated. Similarly to 1-D, the idea is to find which value of the coefficients minimize the difference between the original $\mathbf{u}_h$ and the new approximation $\tilde{\boldsymbol{\mathcal{U}}}_{h,i}$. That is:

$$\tilde{\mathbf{X}}_{\mathcal{A}_i}^{\ell} = \arg\min \left\| \mathbf{u}_h - \tilde{\boldsymbol{\mathcal{U}}}_{h,i} \right\|_{L^2(\mathcal{A}_i)}^2, \tag{52}$$

which leads to the linear system

$$\mathbf{A}_{k,\ell}\, \tilde{\mathbf{X}}_{\mathcal{A}_i}^{\ell} = \mathbf{b}^k, \tag{53}$$

where

$$\mathbf{A}_{k,\ell} = \sum_{\kappa \in \mathcal{A}_i} \left\langle \phi_{\kappa}^k, \phi_{\kappa}^{\ell} \right\rangle_{\kappa}, \tag{54a}$$

$$\mathbf{b}^k = \sum_{\kappa \in \mathcal{A}_i} \left\langle \phi_{\kappa}^k, \mathbf{u}_h \right\rangle_{\kappa}, \qquad k, \ell = 1, \dots, N_p. \tag{54b}$$

By solving the above system for $\tilde{\mathbf{X}}_{\mathcal{A}_i}^{\ell}$ we have completely defined $\tilde{\boldsymbol{\mathcal{U}}}_{h,i}$ within the block $\mathcal{A}_i$. Finally, $\tilde{\mathbf{u}}_{h,i}$ is evaluated by restricting $\tilde{\boldsymbol{\mathcal{U}}}_{h,i}$ just to sub-element κ_i. Namely:

$$\tilde{\mathbf{u}}_{h,i} = \tilde{\boldsymbol{\mathcal{U}}}_{h,i}\Big|_{\kappa_i}, \qquad i = 0, \dots, N_{\text{art}} - 1. \tag{55}$$

4.2. Local multiscale representation of new enriched approximation

The reconstruction methods presented in Section 4.1 allow us to assemble a new more accurate approximation $\tilde{u}_h$ to the exact solution than the original approximation u_h. This new approximation becomes the starting point of the local multiresolution method, as shown in Fig. 3(b). By means of the local MRA we are able to perform an independent two-level multiscale decomposition of $\tilde{u}_h$ for every element $K \in \Omega_h$.

To proceed with the local MRA we remind the reader of the procedure to link the DGM and multiwavelets, as expressed by Eq. (23) and (29) in the one- and two-dimensional context, respectively. Certainly, the 1-D coupling has been illustrated in detail in Fig. 2. However, this previous development is associated to the global multiresolution approach proposed by Hovhannisyan et al. [19] and Gerhard and Müller [22], as the entire domain of the solution undergoes one unique multiscale decomposition. This can be visualized in Fig. 3(a). To adapt the development to our new local MRA we must consider every $K \in \Omega_h$ as harboring one independent multiscale decomposition of $\tilde{u}_h$. Consequently, for the 1-D local MRA we have the element-wise coupling expressed as

$$\tilde{s}_{(\mathcal{M},j)}^{\ell} = 2^{-\mathcal{M}/2}\, \tilde{U}_{(\mathcal{M},j)}^{\ell}, \quad \ell = 1, \dots, N_p, \quad j = 0, \dots, 2^{\mathcal{M}} - 1, \tag{56}$$

where $\tilde{U}_{(\mathcal{M},j)}^{\ell}$ are the coefficients of $\tilde{u}_h$ as calculated by one of the reconstruction methods discussed in the previous section, and $\mathcal{M}$ represents the highest level of resolution within element K. By nature of the two-level multiscale decomposition of $\tilde{u}_h$, $\mathcal{M} = 1$ and we can further simplify Eq. (56) to

$$\tilde{s}_{(1,j)}^{\ell} = \frac{1}{\sqrt{2}} \tilde{U}_{(1,j)}^{\ell}, \qquad \ell = 1, \dots, N_p; \quad j = 0, 1; \tag{57}$$

where the indices $i = j = 0, 1$ coincide with the numbering of the artificial sub-elements κ_i defined in Eq. (32). Therefore, we can establish a relation between the *multiwavelet nomenclature* of Eq. (57) and the *reconstruction terminology* of Eqs. (32) and (33). Namely:

$$\tilde{s}_{\kappa_i}^{\ell} = \frac{1}{\sqrt{2}} \tilde{U}_{\kappa_i}^{\ell}, \qquad \ell = 1, \dots, N_p; \quad i = 0, \dots, N_{\text{art}} - 1; \tag{58}$$

with $N_{\text{art}} = 2$ in the current 1-D setting. We have linked the coefficients of the new enriched approximation, $\tilde{U}_{\kappa_i}^{\ell}$, to the single-scale coefficients, $\tilde{s}_{\kappa_i}^{\ell}$. The remaining lower-level single-scale and multiwavelet coefficients can be obtained by applying the QMF coefficients [35] developed in Eq. (26). They are given by

$$\tilde{s}_K^{\ell} = \sum_{k=1}^{N_p} \sum_{i=0}^{N_{\text{art}}-1} H_{\ell k}^{(i)}\, \tilde{s}_{\kappa_i}^k, \qquad \ell = 1, \dots, N_p; \tag{59a}$$

$$\tilde{d}_K^{\ell} = \sum_{k=1}^{N_p} \sum_{i=0}^{N_{\text{art}}-1} G_{\ell k}^{(i)}\, \tilde{s}_{\kappa_i}^k. \tag{59b}$$

We can observe how the multiscale representation naturally connects the coefficients of the artificial sub-elements κ_i to the coefficients of element K. Finally, the multiscale representation of $\tilde{u}_h$ can be now expressed by Eq. (24) as a combination of single-scale functions and multiwavelets:

$$\tilde{u}_h = \tilde{S}_K + \tilde{D}_K = \sum_{\ell=1}^{N_p} \left(\tilde{s}_K^{\ell} \phi_K^{\ell} + \tilde{d}_K^{\ell}\, \psi_K^{\ell}\right), \qquad K \in \Omega_h. \tag{60}$$

We are particularly interested in how the multiscale information is carried by the multiwavelet contribution, $\tilde{D}_K$. This contribution carries the individual features of the new approximation $\tilde{u}_h$ and, by extension, it becomes an instrument to measure the behavior of the original DG solution u_h. In regions where the solution is regular $\tilde{D}_K$ reports minor or negligible values, whereas regions that harbor discontinuities translate into $\tilde{D}_K$ reaching significant values. Certainly, the works of Hovhannisyan et al. [19] and Shelton [24] have capitalized on the multiwavelet contribution along a hierarchy of multiple levels to perform grid adaptation. Additionally, Vuik [28] has employed this contribution for troubled-cell indication. It is worth mentioning that Vuik also developed a two-level multiscale representation. However, in line with the global MRA philosophy, it is restricted to a sufficiently detailed DG solution u_h^*, as illustrated in Fig. 3(a).

4.2.1. Two-dimensional multiwavelet decomposition

In the two-dimensional setting, Eq. (58) becomes

$$\tilde{\mathbf{s}}_{\kappa_i}^{\ell} = \frac{1}{2} \tilde{\mathbf{U}}_{\kappa_i}^{\ell}, \qquad \ell = 1, \dots, N_p^{2\text{D}}; \quad i = 0, \dots, N_{\text{art}} - 1; \tag{61}$$

where $N_p^{2\text{D}} = (p+1)^2$ and $N_{\text{art}} = 4$. As a reminder, the artificial sub-elements κ_i originate from element K and they have been previously defined in Eq. (48). The QMF coefficients [35] described in Eq. (59) can

be applied to calculate the single-scale coefficients and multiwavelet coefficients along the x-, y- and xy-directions [26]. They read:

$$\tilde{\mathbf{s}}_K^{\ell} = \sum_{i_x,i_y=0}^{1} \sum_{k_x,k_y=1}^{N_p^{1D}} \left[H^{(i_x)}_{\ell_x,k_x} H^{(i_y)}_{\ell_y,k_y} \tilde{\mathbf{s}}^k_{\kappa_i} \right], \tag{62a}$$

$$\tilde{\mathbf{d}}_K^{\ell,\alpha} = \sum_{i_x,i_y=0}^{1} \sum_{k_x,k_y=1}^{N_p^{1D}} \left[G^{(i_x)}_{\ell_x,k_x} H^{(i_y)}_{\ell_y,k_y} \tilde{\mathbf{s}}^k_{\kappa_i} \right], \tag{62b}$$

$$\tilde{\mathbf{d}}_K^{\ell,\beta} = \sum_{i_x,i_y=0}^{1} \sum_{k_x,k_y=1}^{N_p^{1D}} \left[H^{(i_x)}_{\ell_x,k_x} G^{(i_y)}_{\ell_y,k_y} \tilde{\mathbf{s}}^k_{\kappa_i} \right], \tag{62c}$$

$$\tilde{\mathbf{d}}_K^{\ell,\gamma} = \sum_{i_x,i_y=0}^{1} \sum_{k_x,k_y=1}^{N_p^{1D}} \left[G^{(i_x)}_{\ell_x,k_x} G^{(i_y)}_{\ell_y,k_y} \tilde{\mathbf{s}}^k_{\kappa_i} \right], \tag{62d}$$

where

$$i = 2i_x + i_y,$$
$$k = N_p^{1D}(k_x - 1) + k_y, \quad \ell = N_p^{1D}(\ell_x - 1) + \ell_y,$$

with $N_p^{1D} = p + 1$. The link between the coefficients of element K and the coefficients of sub-elements κ_i has been now established. Lastly, the multiscale representation of $\tilde{\mathbf{u}}_h$ resembles Eq. (60) and thus it can be expressed as:

$$\begin{aligned}\tilde{\mathbf{u}}_h &= \tilde{\boldsymbol{S}}_K + \tilde{\boldsymbol{D}}_K^{\alpha} + \tilde{\boldsymbol{D}}_K^{\beta} + \tilde{\boldsymbol{D}}_K^{\gamma} \\ &= \sum_{\ell=1}^{N_p^{2D}} \left(\tilde{\mathbf{s}}_K^{\ell} \boldsymbol{\Phi}_K^{\ell} + \tilde{\mathbf{d}}_K^{\ell,\alpha} \boldsymbol{\Psi}_K^{\ell,\alpha} + \tilde{\mathbf{d}}_K^{\ell,\beta} \boldsymbol{\Psi}_K^{\ell,\beta} + \tilde{\mathbf{d}}_K^{\ell,\gamma} \boldsymbol{\Psi}_K^{\ell,\gamma} \right).\end{aligned} \tag{63}$$

4.3. Novel error estimators based on local MRA

Up to this point, we have described several post-enrichment methods applied to the original DG solution u_h. Thanks to them we have been able to construct a new approximation $\tilde{u}_h$. Subsequent to this step, we have performed a local MRA decomposition of $\tilde{u}_h$ by means of a multiwavelet expansion.

In this section we resume from the local MRA representation. We will evaluate its multiwavelet contribution, $\tilde{D}_K$, to achieve an estimation of the discretization error on element K. The resulting local error estimators constitute a *hybrid* approach between the more traditional *a posteriori* error indicators, e.g. Mavriplis [36], and the more reliable indicators of the global MRA presented in Gerhard et al. [20].

The main idea is to compute the L^2-norm of $\tilde{D}_K$ from Eq. (60), which can be read as an evaluation of the *energy* associated to the individual fluctuations of $\tilde{u}_h$. Consequently, in the 1-D context the underlying structure of the local indicators can be expressed as:

$$\begin{aligned}\eta_K &= \left\| \tilde{D}_K \right\|_{L^2(K)} \\ &= \left\| \sum_{\ell=1}^{N_p} \tilde{d}_K^{\ell} \psi_K^{\ell} \right\|_{L^2(K)} \\ &= \left[\sum_{\ell=1}^{N_p} \left(\tilde{d}_K^{\ell} \right)^2 \right]^{1/2}, \qquad K \in \Omega_h,\end{aligned} \tag{64}$$

where $\langle \psi_K^{\ell}, \psi_K^{\ell'} \rangle_K = \delta_{\ell,\ell'}$ derived from the orthonormality relations in Eq. (17) has been used to simplify the final expression.

With this framework in mind, we propose three error indicators in total. The difference between them lies in the reconstruction method employed to reach $\tilde{u}_h$ and their terminology reflects this fact (see Sections 4.1.1 to 4.1.3). Consequently, we rewrite Eq. (64) to account for the post-enrichment procedure. Namely:

r-multiwavelet indicator, $\eta_K^{r\text{-MW}}$,

with

$r \in \{\kappa\text{-}, K\text{-}, \Gamma\text{-reconstruction}\}, \quad K \in \Omega_h,$

where index r may refer to method ①, ②, or ③from Fig. 4, respectively.

4.3.1. Two-dimensional indicator

Similarly to the 1-D setting, we will evaluate the multiwavelet contribution resulting from applying a local MRA to the new approximation $\tilde{\mathbf{u}}_h$ as an assessment of the discretization error on element K. However, in the 2-D context only one error indicator will be developed. This indicator will be based on the κ-reconstruction procedure presented in Section 4.1.4 and its terminology will be adapted accordingly.

Hence, the *κ-multiwavelet* indicator is defined by evaluating the x-, y- and xy- components of the multiwavelet contribution given by Eq. (63) in the L^2-norm. Namely:

$$\begin{aligned}\eta_K^{\kappa\text{-MW}} &= \left\| \tilde{\boldsymbol{D}}_K^{\alpha} + \tilde{\boldsymbol{D}}_K^{\beta} + \tilde{\boldsymbol{D}}_K^{\gamma} \right\|_{L^2(K)} \\ &= \left\| \sum_{\ell=1}^{N_p} \left(\tilde{\mathbf{d}}_K^{\ell,\alpha} \boldsymbol{\Psi}_K^{\ell,\alpha} + \tilde{\mathbf{d}}_K^{\ell,\beta} \boldsymbol{\Psi}_K^{\ell,\beta} + \tilde{\mathbf{d}}_K^{\ell,\gamma} \boldsymbol{\Psi}_K^{\ell,\gamma} \right) \right\|_{L^2(K)},\end{aligned} \tag{65}$$

where $K \in \Omega_h$ and $N_p = N_p^{2D} = (p+1)^2$. In general, if we extend the orthonormality relations in Eq. (17) to the current 2-D setting and consider the extra directions given by the superscripts α, β, and γ we have the following new orthonormality relations:

$$\left\langle \boldsymbol{\Psi}_K^{\ell,\alpha}, \boldsymbol{\Psi}_K^{k,\alpha} \right\rangle_K = \delta_{\ell,k}, \quad \left\langle \boldsymbol{\Psi}_K^{\ell,\alpha}, \boldsymbol{\Psi}_K^{k,\beta} \right\rangle_K = \left\langle \boldsymbol{\Psi}_K^{\ell,\alpha}, \boldsymbol{\Psi}_K^{k,\gamma} \right\rangle_K = 0, \tag{66a}$$

$$\left\langle \boldsymbol{\Psi}_K^{\ell,\beta}, \boldsymbol{\Psi}_K^{k,\beta} \right\rangle_K = \delta_{\ell,k}, \quad \left\langle \boldsymbol{\Psi}_K^{\ell,\beta}, \boldsymbol{\Psi}_K^{k,\alpha} \right\rangle_K = \left\langle \boldsymbol{\Psi}_K^{\ell,\beta}, \boldsymbol{\Psi}_K^{k,\gamma} \right\rangle_K = 0, \tag{66b}$$

$$\left\langle \boldsymbol{\Psi}_K^{\ell,\gamma}, \boldsymbol{\Psi}_K^{k,\gamma} \right\rangle_K = \delta_{\ell,k}, \quad \left\langle \boldsymbol{\Psi}_K^{\ell,\gamma}, \boldsymbol{\Psi}_K^{k,\alpha} \right\rangle_K = \left\langle \boldsymbol{\Psi}_K^{\ell,\gamma}, \boldsymbol{\Psi}_K^{k,\beta} \right\rangle_K = 0. \tag{66c}$$

where $\ell, k = 1, \ldots, N_p$. Consequently, Eq. (65) can be simplified to

$$\eta_K^{\kappa\text{-MW}} = \left[\sum_{\ell=1}^{N_p} \left(\tilde{\mathbf{d}}_K^{\ell,\alpha} \right) + \sum_{\ell=1}^{N_p} \left(\tilde{\mathbf{d}}_K^{\ell,\beta} \right) + \sum_{\ell=1}^{N_p} \left(\tilde{\mathbf{d}}_K^{\ell,\gamma} \right)^2 \right]^{1/2}, \quad K \in \Omega_h. \tag{67}$$

4.4. Element marking strategies

Once we have determined the set of local error estimates η_K for every $K \in \Omega_h$, we now will use this information to select (*mark*) which elements require higher spatial resolution (h-refinement). Note that the error estimates could be used to identify elements which require lower spatial resolution (h-coarsening) as well. However, element agglomeration will not be considered in this study.

There are numerous marking strategies developed in the literature. Based on the findings of Naddei [9] we have opted for the two following procedures:

(a) *Local threshold strategy*. It is the most intuitive and widely used strategy (see e.g. Oden et al. [40] or Rueda-Ramírez et al. [41]). The idea is to flag an element K if the local value of the error indicator η_K is above a user-defined tolerance, η_{tol}. Therefore, we define the set of marked elements, Λ, as follows:

$$\Lambda = \left\{ K \in \Omega_h \mid \eta_K > \eta_{\text{tol}} \right\}. \tag{68}$$

For this strategy, the selection of appropriate tolerances is influenced by the characteristics of the flow under study. Therefore, the experience of the user plays a significant role in the decision process. However, we can recommend basic instructions on how to select some preliminary values. For instance, when using the multiwavelet indicator in Eq. (67), the error estimator delivers a mean value of the fluctuations of a given physical quantity (e.g. momentum density, pressure, vorticity) within the confines of the element. Consequently, we can set a percentage of the pertinent reference quantity as an appropriate tolerance.

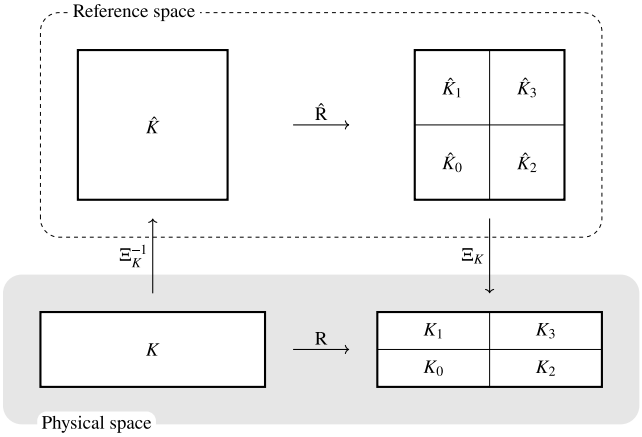

Fig. 5. Isotropic h-refinement in the context of reference and physical element.

(b) *Maximum marking strategy*. Initially proposed by Babuvška and Rheinboldt [42], it has seen widespread adoption (see e.g. Dörfler and Heuveline [43]). In this case, K is flagged if η_K is above a specified percentage of its maximum. Namely:

$$\Lambda = \left\{ K \in \Omega_h \mid \eta_K > \theta \max_{K \in \Omega_h} \eta_K \right\}, \tag{69}$$

where the user-defined parameter $\theta \in [0, 1]$ is called *marking fraction*. The lower this parameter, the higher the number of total marked elements.

In addition, we limit the separation in refinement levels between neighboring elements to at most one by marking additional elements if necessary. This is frequently called the *two-to-one* rule [44] and safeguards that neighboring elements are not of exceedingly dissimilar size.

4.5. Element refinement strategy

After selecting the elements that require higher spatial resolution by one of the proposed marking strategies, we proceed to the construction of the new (adapted) mesh. For that purpose, we follow the so-called *local mesh refinement* strategy [45], which restrict the adaptation to individual marked elements. This is in contrast to *semi-local* approaches such as AMR [46], in which elements of one or more regions of the mesh are refined as a group.

The element refinement strategy pursued in this study is based on the work by Kuru et al. [47] and Naddei [9], where they have implemented an (isotropic) local mesh refinement strategy on non-conforming curvilinear hexahedral and quadrilateral meshes. Their idea is to divide each of the marked elements into 2^d new elements, where d is the dimension of the problem.

In our case, we consider simpler non-conforming Cartesian meshes in 2-D. Consequently, elements become rectangles that, if marked for refinement, may produce four new geometrically similar rectangles. To visualize this concept let $\mathcal{G}_0 = \Omega_h$ be the given initial mesh and $\mathcal{G}_1$ be the resulting mesh after refinement. We denote any $K \in \Lambda$ with $\Lambda \subset \mathcal{G}_0$ by a *parent* element. Its associated *child* elements are denoted by the set $\{K_j\}_{j=0}^{3} \in \mathcal{G}_1$. Then, thanks to the refinement operator $\mathrm{R} : \{K\} \to \{K_0, \dots, K_3\}$ we can explicitly define the link between parent and children in physical space. The operator R can be further expressed in the reference space as follows:

$$\mathrm{R} = \Xi_K \hat{\mathrm{R}}\, \Xi_K^{-1} \tag{70}$$

where $\hat{\mathrm{R}} : \{\hat{K}\} \to \{\hat{K}_0, \dots, \hat{K}_3\}$ denotes the operator that divides the reference element into four identical children, and Ξ_K is a linear transformation that maps elements of the reference space, $\hat{K} \in \hat{\Omega}_h$, to elements of the physical space, $K \in \Omega_h$. Further to this, because we work with rectangles, the mapping function is simply a scaling of the reference space. Fig. 5 describes the procedure in detail.

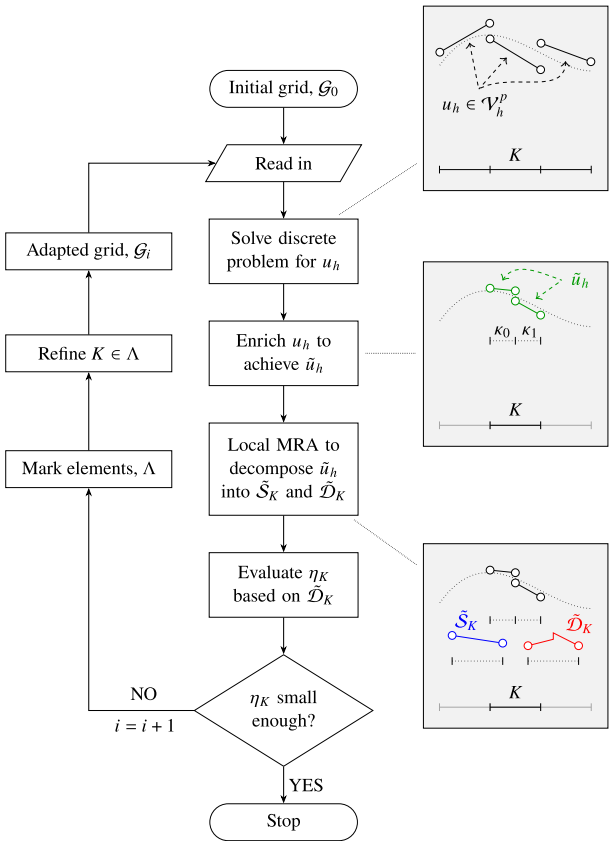

Fig. 6. Flow chart of the proposed h-adaptive algorithm.

4.6. The h-adaptive algorithm

A flow chart describing our h-refinement algorithm for steady problems is shown in Fig. 6. The diagram describes adaptation in the 1-D context, but the extension to 2-D is straightforward. The algorithm consists of first providing an initial mesh and solving for the corresponding DG approximate solution. Next, the approximation is subjected to a series of post-processing steps. Firstly, we build a more accurate approximate solution by employing the reconstruction methods described in Section 4.1. Secondly, we perform a local multiscale decomposition of the reconstruction to extract its multiwavelet contribution, as explained in Section 4.2. Lastly, we construct the local error estimator based on the multiwavelet contribution, as presented in Section 4.3. This estimation offers an insight into the quality of the solution and thus it determines if the spatial resolution must be upgraded. If that is the case, we proceed to flag the elements that demand higher resolution according to the marking strategies identified in Section 4.4. We then refine those elements by following the guidelines presented in Section 4.5 to arrive to the adapted mesh. The discrete problem for the new mesh is solved again and the entire procedure is repeated until certain error criteria are fulfilled.

Generally, two extra steps are applied directly after obtaining the new refined mesh. The first step is the so-called *reinitialization* operation. It means that the L^2-projection of the previous solution is used as the initial condition on the new mesh. The second step is *load balancing* in the context of parallel computations. This operation leads to a uniform distribution of the computational load by efficiently partitioning the new mesh.

5. Numerical results

In the following, the different error estimation strategies developed in Section 4.3 will be assessed and compared against relevant indicators from the literature. Our objective is to evaluate their overall performance in the context of *h*-adaptive simulations, first in the one dimensional case for the viscous Burgers equation and then in two dimensions for compressible Navier–Stokes considering a laminar flow over a backward-facing step.

5.1. One-dimensional viscous Burgers equation

Based on the viscous Burgers equation, which has been described in detail in Appendix, we perform a series of steady simulations on the computational domain $\Omega_h = [-1, 1]$. We cover two configurations with different initial conditions (ICs) and boundary conditions (BCs). Firstly, a stationary front (IC-*shock*) which simulates the presence of a sharp gradient in the middle of the domain. For this configuration we have $u(x,0) = -\tanh(x/2\nu)$ with $\nu = 0.02$ and $u(\mp 1, t) = \pm 1$. These conditions are analogous to the solution of the Riemann problem for large enough $t > 0$. The second configuration is determined by a sinusoid and it is representative of a smooth solution (IC-*smooth*). Thus we define $u(x,0) = \sin(2\pi x)$ and $u(\mp 1, t) = 0$. To avoid the development of sharp gradients, a source term is added to the formulation by the method of *manufactured solutions*. Namely:

$$S(x) = (2\pi)\sin(2\pi x)\cos(2\pi x) + \nu(2\pi)^2 \sin(2\pi x). \tag{71}$$

To evolve the solution in time from either of the initial conditions up to the steady-state, the explicit scheme in Eq. (A.7) is employed. We then apply recursively the *h*-adaptive algorithm explained in Section 4.6 and Fig. 6 until we achieve the desired adapted solution.

The *h*-adaptive algorithm determines if refinement is required based on the value provided by an error estimator in conjunction with the *local threshold* marking strategy described by Eq. (68) in Section 4.4. We center our computations on the three multiwavelet-based error estimation strategies developed in Section 4.3 and derived from Eq. (64). We remind the reader of the terminology of these indicators:

1. κ-*multiwavelet* indicator, denoted by $\eta_K^{\kappa\text{-MW}}$.
2. *K*-*multiwavelet* indicator, symbolized by $\eta_K^{K\text{-MW}}$.
3. Γ-*multiwavelet* indicator, given by $\eta_K^{\Gamma\text{-MW}}$.

We also include from the literature two indicators extensively tested in Naddei et al. [7,8] and Naddei [9] so that we can compare them against the MW-based indicators. We consider the *small-scale energy density* (SSED) indicator [7,47] and the *spectral decay* (SD) indicator [48]. The SSED measures the energy associated with the highest-order modes. It is expressed as:

$$\eta_K^{\text{SSED}} = \left\| \sum_{\ell=1}^{N_p} U_K^\ell \phi_K^\ell - \sum_{\ell=1}^{N_p-1} U_K^\ell \phi_K^\ell \right\|_{L^2(K)}. \tag{72}$$

The SD corresponds to the SSED indicator normalized by the total energy within the element. That is:

$$\eta_K^{\text{SD}} = \frac{\left\| \sum_{\ell=1}^{N_p} U_K^\ell \phi_K^\ell - \sum_{\ell=1}^{N_p-1} U_K^\ell \phi_K^\ell \right\|_{L^2(K)}}{\left\| \sum_{\ell=1}^{N_p} U_K^\ell \phi_K^\ell \right\|_{L^2(K)}}. \tag{73}$$

In the following we define several quantities that will be used to better understand the numerical results. Let u be the exact solution to the viscous Burgers equation and $u_h \in \mathcal{V}_h^p$ its approximate DG solution. We define the discretization error as follows:

$$\|e_h\|_{L^2(\Omega)} = \|u - u_h\|_{L^2(\Omega)}. \tag{74}$$

Additionally, we measure the difference between the approximate DG solution u_h and the reconstruction $\tilde{u}_h \in \mathcal{V}_h^p$ by:

$$\|\mathcal{E}_h\|_{L^2(\Omega)} = \|\tilde{u}_h - u_h\|_{L^2(\Omega)}, \quad \text{with } \tilde{u}_h = \sum_K \tilde{u}_{h|K}, \ \forall K \in \Omega_h, \tag{75}$$

which follows the nomenclature in Dolejší and Solin [32]. The authors set Eq. (75) as their estimation of the discretization error. We call this measure the *Dolejší estimation*. In our case, the value of $\tilde{u}_h$ is given by the reconstruction methods described in Section 4.1. Therefore, we have three versions of the Dolejší estimation, corresponding to the three post-enrichment methods studied. They are denoted by $\mathcal{E}_h^\kappa$, $\mathcal{E}_h^K$, and $\mathcal{E}_h^\Gamma$. The Dolejší estimation becomes another entry to the comparison between the multiwavelet-based indicators and the SSED and SD indicators.

Finally, we define the *effectivity index* as the ratio between the error given by the indicator and the discretization error. It reads

$$\iota^{\text{eff}} = \frac{\eta}{e_h}, \tag{76}$$

where $\eta = \left(\sum_{K\in\Omega_h} \eta_K^2\right)^{1/2}$. This index is a measure of the quality of the error estimation. An index close to unity means that the estimator accurately mimics the evolution of the discretization error. For each computation of the *h*-adaptive algorithm, we evaluate the error estimator over the full domain, η; the discretization error, e_h; and the Dolejší estimation, $\mathcal{E}_h$. In addition, we evaluate the effectivity index for selected cases.

An analysis of the effect of the indicators in the adaptation of the viscous Burgers equation under IC-*shock* is plotted in Fig. 7 for different degrees p of the numerical solution. Figs. 7(a), 7(b), and 7(c) show the variation of the discretization error e_h in the conservative variable u versus the number of degrees of freedom (#DOFs) when uniform *h*-refinement is performed as well as for the locally *h*-adapted solution under the different error estimators. For every analyzed degree, the error associated with the uniform *h*-refinement follows the theoretical slope representing the order of the method, as illustrated by the dashed lines. With respect to the adaptive procedure, all the indicators lead to a large decrease in the #DOFs for a given level of accuracy. The SSED and SD indicators show a marginally faster reduction of the #DOFs during the initial refinement steps. However, the multiwavelet-based indicators display a slightly better performance in the last refinement steps, especially at lower degrees of the approximation. They achieve savings in #DOFs of about 85% in $p = 1$, see Fig. 7(a), whereas the SSED and SD indicators show a reduction of around 81% for the same degree. The savings are scaled down to 77% for the MW-based indicators and 75% for the SSED and SD indicators when the degree is increased to $p = 3$, as can be seen in Fig. 7(c). This shows that the higher the degree, the closer is the behavior of the MW-based indicators to the SSED and SD indicators. Indeed, the difference in the savings of #DOFs goes from 4% to 2% when jumping from $p = 1$ to $p = 3$. Overall, the evolution of the MW-based indicators closely resembles the behavior of the indicators from the literature while showing slightly larger savings at lower degrees. This low-order outcome is expected, as the SSED and SD indicators are known to underperform at low-orders of the approximation [9]. These results yield a validation of our proposed estimators.

Finally, in the same figures we observe that the different Dolejší estimations behave similarly to their homologous MW-based error estimators. This further validates the idea of using reconstruction techniques as an important tool in mesh adaptation. At this point, the question of why using a multiwavelet expansion which is computationally more expensive than a direct comparison between the original DG solution and a post-enriched solution may arise. The answer resides in the fact that the multiwavelet expansion yields more detailed information about the solution and its local regularity. This is especially true in higher dimensions, where the details are directly given component-wisely. Moreover, studies of the effectivity index (not presented in this work) show a behavior closer to unity when employing the multiwavelet decomposition. Hence, these reasons motivate the use of a multiwavelet expansion to compute the indicators.

We now focus our attention on the final *h*-adapted mesh resulting from the activation of the three different local multiwavelet-based

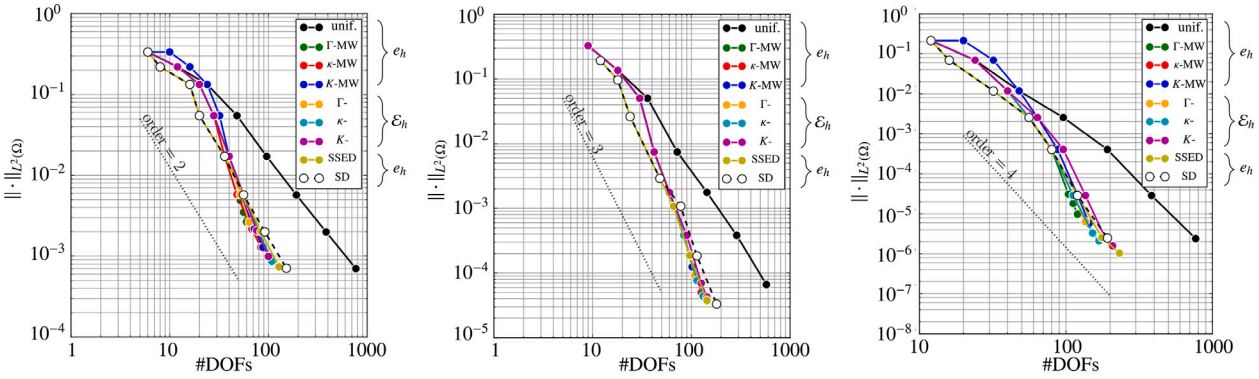

(a) $p = 1$. (b) $p = 2$. (c) $p = 3$.

Fig. 7. Viscous Burgers equation with IC-*shock*. Discretization error in L^2-norm under uniform and h-adaptive refinement for selected orders of the numerical solution. Adaptation is guided by various estimators. The multiwavelet family of estimators, Eq. (64), is denoted by ● ● ●, the estimators from the literature, Eqs. (72) and (73), are symbolized by ● ○, and the Dolejší estimation, Eq. (75), is showcased by ● ● ●. For all estimators, the adaptive process is performed up to the 7th adaptation step.

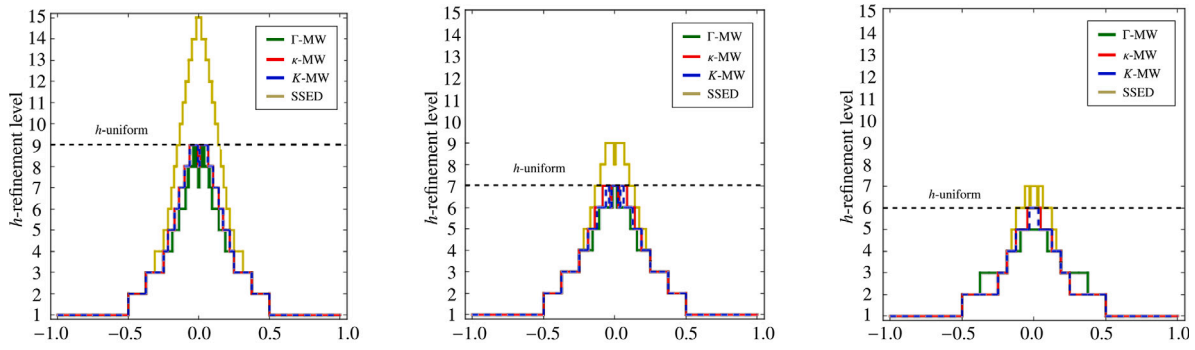

(a) $p = 1$ (b) $p = 2$. (c) $p = 3$.

Fig. 8. Viscous Burgers equation with IC-*shock*. Different levels of refinement achieved by every error estimator at the last iteration step for selected solution orders. The dashed line corresponds to an uniform mesh with discretization error $\|e_{h|K}\| < \eta_{\text{tol}}$ for all $K \in \Omega_h$ where $\eta_{\text{tol}} = 1 \times 10^{-6}$. The adaptive process is then performed for each estimator until we achieve $\eta_K < \eta_{\text{tol}}$ in every element of the domain.

indicators proposed in this research. We have just seen that the SSED indicator shows a slightly better agreement with our indicators compared to the SD. Thus from now on we will only use the SSED indicator for comparison purposes. The distribution of the refinement levels along the computational domain for each indicator are plotted in Figs. 8(a), 8(b), and 8(c) for $p = 1$, $p = 2$, and $p = 3$, respectively. It can be observed that, predictably, the area surrounding the discontinuity is subjected to a higher level of refinement. This is true for every estimator. When we increase the degree of the solution, the number of refinement levels decreases. This behavior is expected because we are increasing the spatial resolution by modifying the local polynomial degree and thus fewer elements are required to achieve a prescribed level of accuracy. The dashed line represents the required refinement level of an uniform mesh to reach the user defined tolerance η_{tol} =1e-6. The activation of the K-multiwavelet and κ-multiwavelet indicators leads to an almost identical pattern of refinement centered around the discontinuity, regardless of the degree. The Γ-multiwavelet indicator seems to perform marginally better by generating a narrower refined region surrounding the discontinuity. In the case of the SSED indicator, the wider refined region translates into a higher amount of #DOFs compared the MW-based indicators. Again, this is due to the better performance of the MW-based estimators in the last refinement steps. Certainly, they never surpass the dashed line. This behavior is ideal because this means that their highest refinement level remains below the level of the uniform mesh imposed by the tolerance η_{tol}. For the SSED indicator the behavior is different, it exceeds the fixed tolerance leading to an over-refined mesh. Particularly severe is the behavior for $p = 1$, surpassing six levels above η_{tol}. The over-refinement is mitigated by using $p = 3$, in which the difference is reduced to one level. This behavior is closely related to the effectivity index, as we will discuss in the next paragraph.

A closer look at the evolution of the discretization error for the $p = 3$ adapted and uniform grid solutions for the initial condition IC-*shock* is illustrated in Fig. 9. In this case the error on the adapted mesh is compared to the value given by the indicator. If these values show a similar evolution along the refinement process, then the effectivity index associated with the indicator, ι^{eff}, is close to unity. That is $\eta \simeq e_h$. It is understood that values of the effectivity index close to unity are desirable for *a posteriori* indicators (see e.g. error estimation for elliptic problems in Babuvška and Rheinboldt [49]). However, when dealing with hyperbolic or parabolic problems such as the viscous Burgers equation, you may come up with possibly less precise estimates and assume effectivity indices higher than unity (see e.g. Johnson [50]).

Fig. 9(a) presents the estimated error computed by the Γ-multiwavelet indicator versus the #DOFs corresponding to each iteration of the adaptation process. The indicator reports an effectivity index between $0.4 < \iota^{\text{eff}} < 0.7$ during the first iterations. Then progressively drops to $\iota^{\text{eff}} = 0.3$ in the last steps of refinement. The same behavior is observed in Fig. 9(b) for the K-multiwavelet indicator. However, the first refinement steps report a poor effectivity index for this indicator, which may explain the error overshoot on the adapted mesh. After the first iterations, the effectivity index gradually improves until achieving values close to unity in the last refinement steps. Moving to the κ-multiwavelet indicator, Fig. 9(c), we observe a more uniform behavior. Except during the first steps of refinement, the effectivity index remains mostly constant at $\iota^{\text{eff}} = 2$. The estimation mimics the behavior of

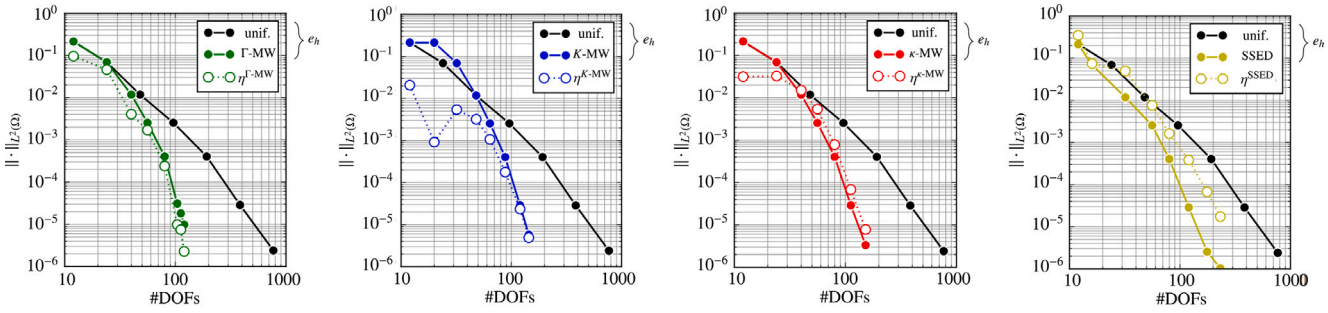

(a) Γ-multiwavelet indicator. (b) K-multiwavelet indicator. (c) κ-multiwavelet indicator. (d) SSED indicator.

Fig. 9. Viscous Burgers equation with IC-*shock* and $p = 3$. Error estimator performance under h-adaptation. We compare the discretization error (solid line) versus the estimation reported by the indicator (dashed line).

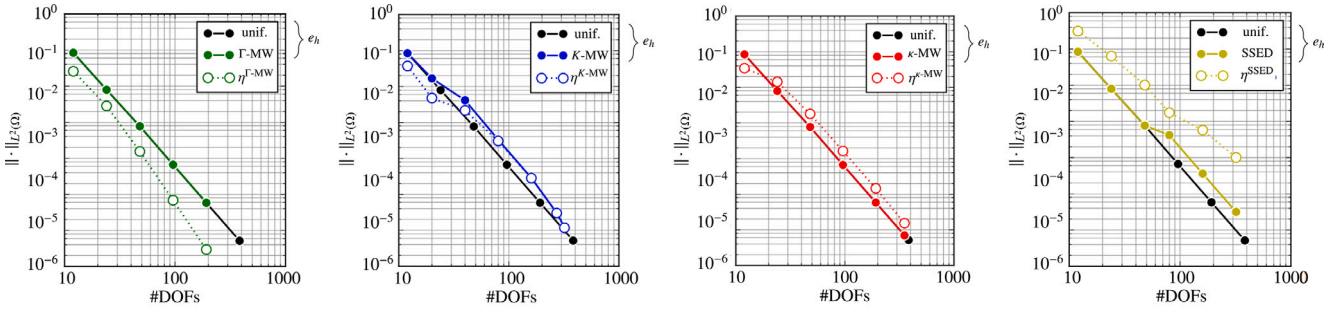

(a) Γ-multiwavelet indicator. (b) K-multiwavelet indicator. (c) κ-multiwavelet indicator. (d) SSED indicator.

Fig. 10. Viscous Burgers equation with IC-*smooth* and $p = 3$. We measure the discretization error (solid line) against the estimation reported by the indicator (dashed line) to evaluate the performance of the said indicator.

the discretization error, while remaining slightly higher. Lastly, the SSED indicator displayed in Fig. 9(d) reports an erratic behavior, with a precise estimate during the first refinement steps and effectivity ratios progressively deteriorating to $\iota^{\text{eff}} > 10$. This behavior may justify the over-refining observed in Fig. 7.

Before drawing any conclusion, it is worth studying the behavior of the indicators for a more regular solution. A further analysis of the effectivity index for the initial conditions IC-*smooth* and $p = 3$ is performed in Fig. 10. This example shows no difference between the use of the uniform and the adapted mesh. This is a consequence of the regularity of the solution. In this situation, performing adaptation is not justified because the final adapted grid is nearly indistinguishable from the uniform mesh. However, a few interesting conclusions can be extracted from this analysis. Firstly, the Γ-multiwavelet indicator, displayed in Fig. 10(a), behaves inadequately when the solution is smooth. In this case, the effectivity index steadily drops to $\iota^{\text{eff}} < 0.1$ in the last steps of refinement. It seems that the influence of the jump of the conservative quantity at the interface between elements is not well captured by the reconstruction. Thus the disparity between estimation and discretization error. Secondly, the K-multiwavelet indicator, illustrated in Fig. 10(b), follows the discretization error particularly well, with $\iota^{\text{eff}} = 1$ during the last steps of refinement. However, a slight overshoot of the estimator appears in the first stage of the refinement. This has been likely caused by under-refining during the early steps. If we pay attention to previous results in reported in Fig. 9(b), we can resolve that the K-multiwavelet indicator is prone to this sort of behavior. The same overshoot can be observed for the SSED indicator, Fig. 10(c), though happening at later stage. This indicator continues to report high values of the effectivity index, $\iota^{\text{eff}} > 10$, similarly to what we observed when IC-*shock* was studied. Finally, the κ-multiwavelet indicator, Fig. 10(d), maintains its characteristic regular behavior with a nearly constant $\iota^{\text{eff}} = 2$ and a satisfactory tracking performance.

From the analysis of Figs. 9 and 10 we thus conclude that the multiwavelet-based indicators constitute a consistent approach for tracking the discretization error of the DG approximation. They perform substantially better than the SSED indicator provided by the literature, which shows an excessively high value of the effectivity index. In particular, the κ-multiwavelet indicator features a regular behavior while maintaining an acceptable effectivity index so that it can be reliably used to control the adaptation process. Based on this analysis, the κ-multiwavelet indicator has been selected to drive the h-adaptive algorithm in the study of the two-dimensional backward-facing step flow.

5.2. Laminar flow over a backward-facing step

In this section a series of numerical simulations of a two-dimensional steady laminar incompressible flow over a backward-facing step are performed to assess the validity of our novel error estimator for efficient mesh adaptation.

The geometry of the computational domain is outlined in Fig. 11(a). Following the work of Barton [51], an extra inlet channel has been considered to ameliorate the influence of the step in the upstream flow region. Similarly, Erturk [52] has concluded that its length must be at least five times the height of the step to be effective. Thus we have sized our inlet channel accordingly. With regard to the outlet or exit boundary, it must be located at a distance sufficiently far away from the step so that the flow becomes fully developed. Similar studies by Keskar and Lyn [53] and Gartling [54] have found that placing the exit boundary at 60 step heights downstream from the step is sufficient to recover a fully developed flow. Therefore, we have sized our expanded channel in accordance. The height of the inlet channel is equal to the dimension of the step, and the channel height in the expanded region (downstream of the step), H, is twice the height of the step, h. Therefore, the expansion ratio of the backward-facing step results in $H/h = 2$. The Reynolds number of the problem is $Re = 800$ and defined as $Re = \frac{UH}{\nu}$, where U is the inlet mean velocity,

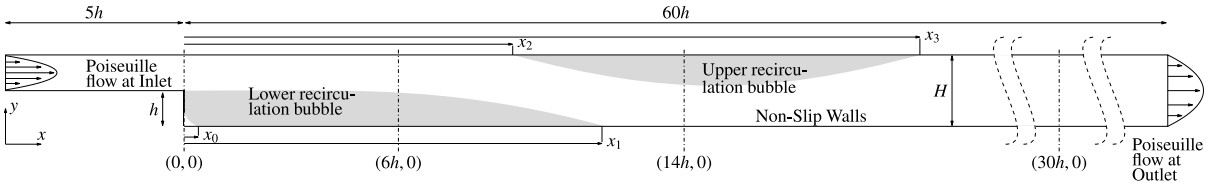

(a) Computational domain and boundary conditions.

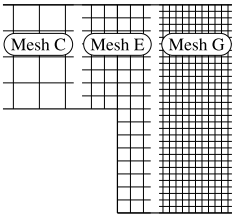

(b) Illustration of uniform grids employed.

Mesh	#Elts	#DOFs			#Elts−y	#DOFs−y		
		$p=1$	$p=2$	$p=3$		$p=1$	$p=2$	$p=3$
A	536			8576	4			16
B	1206		10 854		6		18	
C	2144	8576		34 304	8	16		32
D	4554		40 986		12		36	
E	8096	32 384		129 536	16	32		64
F	18 000		162 000		24		72	
G	32 000	128 000		512 000	32	64		128
H	72 000		648 000		48		144	
I	128 000	512 000		2 048 000	64	128		256
J	288 000		2 592 000		96		288	
K	512 000	2 048 000	4 608 000		128	256	384	

(c) Number of elements (#Elts) and degrees of freedom (#DOFs) for every uniform grid in the study, both in total and along the y-direction (#Elts−y and #DOFs−y) of the expanded channel. Color grouping refers to an approximate equivalence in the #DOFs between different orders in the computations.

Fig. 11. Description of the backward-facing step.

i.e. two thirds of the maximum inlet velocity. Lastly, to insure the incompressibility of the problem the Mach number is set to $Ma = 0.1$.

Regarding the boundary conditions, we impose at the inlet boundary a fully developed plane Poiseuille flow so that the velocity profile at the entrance of the domain is parabolic. At the exit boundary, a non-reflecting boundary condition is imposed such that the velocity profile of the numerical solution at the exit boundary matches the analytical parabolic profile of a Poiseuille flow. Finally, wall boundary conditions are imposed on the upper and bottom walls of the channel, as well as on the surface of the step. The details regarding the considered configuration are reported in Fig. 11(a).

To mesh the domain we have considered 11 different Cartesian uniform grids, depending on the order of the numerical solution at hand. Fig. 11(c) describes the configurations in detail. The grids are named A to K, and ordered by increasing resolution. A sample of the meshes C, E and G is displayed in Fig. 11(b). The grids A, B and C (gray shaded cells) correspond to the three initial computational grids from which the adapted grids will be built. They represent the coarsest starting meshes for $p = 1$, $p = 2$, and $p = 3$, respectively. The grid K with $p = 2$ (boxed cell) corresponds to the reference solution of the present study. Those grids that retain an equivalent number of degrees of freedom (#DOFs) for different orders in the computations are labeled with the same color nomenclature. That means that their numerical solution should be comparable between computations based on different polynomial orders. Fig. 11(c) also reports how this equivalence in #DOFs is maintained along the y-direction of the expanded channel. The uniform grids obviously display the same #DOFs per unit distance in both x- and y-direction. Finally, for the coarser meshes (grids A to E), the region immediately after the inlet has been locally refined so that we are able to properly capture the parabolic inflow from the initial steps of the adaptation process and therefore impose an appropriate inlet profile. Indeed, the study by Yee et al. [55] shows that when a coarse grid is employed in the backward-facing step flow at $Re = 800$, a spurious oscillating numerical solution is obtained and the steady-state cannot be reached. The work of Erturk [52], in which an interval of $Re = [100, 3000]$ is investigated by solving the flow using a second order finite difference method, employs a very fine mesh so that convergence to the steady-state can be achieved. For the meshes employed in this work, and the polynomial orders considered in the DGM used, the convergence problems reported by Yee et al. [55] were not encountered, even for solutions with low polynomial degrees such as $p = 1$.

To evaluate the quality of our numerical solution, we have selected three streamwise locations along the expanded channel, as reported in Fig. 11(a). They cover the lower and upper recirculation bubbles ($x = 6h$ and $x = 14h$), and an overview of the developed flow far away downstream ($x = 30h$). The idea is to extract the profiles of the relevant physical quantities along the vertical direction of the main channel. We will consider the profiles of the horizontal and vertical components of the velocity, given by u and v. The profile vorticity, defined as $\omega = \partial v/\partial x - \partial u/\partial y$, is also included in the analysis. These profiles are examined and compared to the results from the study of Erturk [52] at the same streamwise locations. In that study, the author uses a grid of 101 uniform elements along the vertical direction of the expanded channel and their scheme is second order accurate. Thus we count 202 DOFs along the y-direction. In comparison, we have described our reference solution as a third order numerical solution with 384 DOFs along the same direction (see Fig. 11(c)).

The results comparing the solution obtained by Erturk versus our reference solution are shown in Fig. 12. We observe that our computed profiles agree well with those of the literature for every physical quantity analyzed. There are small discrepancies in the maximum values of the x- and y- velocities. We believe this is due to the fact that in our simulations the maximum x-velocity of the parabolic profile is slightly higher right at the fall of the step than at the upstream inlet. However, Erturk shows that for $Re = 800$, these two profiles must be nearly identical. We think that by using a compressible solver (for an incompressible flow) it makes it much harder to adjust the inflow/outflow boundary conditions to attenuate the small increase in the horizontal velocity at the step. We consider that this slight deviation does not substantially affect the outcome of the h-adaptation analysis, which is the main focus of our study.

After validating the numerical results on uniform grids, we now investigate how to reduce the grid size locally, and thus the computational load, for a given level of accuracy. The idea is to start from a coarse mesh, such as the mesh A, B or C reported in Fig. 11(c), and to detect the regions in which the approximate DG solution is underresolved and a finer local mesh resolution might be required. To that end, the h-adaptive algorithm described in Section 4.6 is applied repeatedly until the desired adapted solution is reached. To select those elements that require higher resolution for each iteration we use an error estimator (Section 4.3) in conjunction with an appropriate marking strategy (Section 4.4).

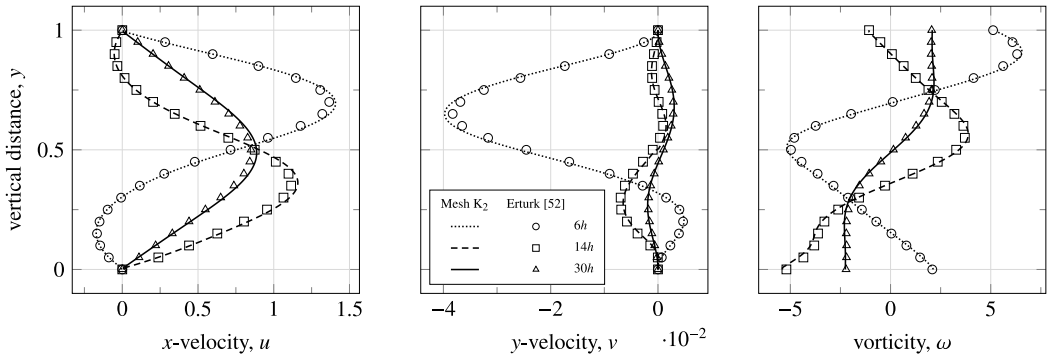

Fig. 12. Laminar backward-facing-step. Profiles for different physical quantities at three different streamwise locations along the expanded channel. The profiles have been extracted from our reference numerical solution (mesh K with $p = 2$) and compared with the literature at the same locations.

Next, we will enumerate the error estimators employed for this configuration, and later we will stress the importance of a suitable marking strategy associated to the estimation. We focus our computations on the κ-multiwavelet indicator as defined by Eq. (67). This choice of the error estimator was justified by the encouraging results reported from the computations of the 1-D viscous Burgers equation in Section 5.1, where it proved to have the best overall behavior. The κ-multiwavelet indicator may be evaluated for every conservative variable $\mathbf{u} = (\rho, \rho\mathbf{v}, \rho E)$ or any other derived quantity. For the study of the backward-facing step we have selected the horizontal and vertical components of the momentum density vector ($\rho\mathbf{v}$), the pressure (p), and the vorticity (ω). They constitute relevant quantities representative of the behavior of the overall solution. Therefore we come up with three different variations of the multiwavelet-based indicator that will be used in the computations, namely:

1. κ-multiwavelet *on density momentum* indicator (MW-$\rho\mathbf{v}$), denoted by $\eta_K^{\text{MW-}\rho\mathbf{v}}$.
2. κ-multiwavelet *on pressure* indicator (MW-p), given by $\eta_K^{\text{MW-}p}$.
3. κ-multiwavelet *on vorticity* indicator (MW-ω), symbolized by $\eta_K^{\text{MW-}\omega}$.

It is worth mentioning that we have dropped the "κ-" terminology when symbolizing the new indicators to simplify the nomenclature. However, we remind the reader that when denoting MW-based indicators in this section, we exclusively refer to the κ-multiwavelet indicator applied to selected conservative and derived quantities.

Similarly to the one-dimensional configuration in Section 5.1, the small-scale energy density (SSED) and spectral decay (SD) error estimators will be once more compared to the multiwavelet-based indicators. In the two-dimensional setting, they are defined as [7]:

$$\eta_K^{\text{SSED}} = \frac{\left\| (\rho\mathbf{v})_p - (\rho\mathbf{v})_{p-1} \right\|_{L^2(K)}}{|K|^{1/2}}, \tag{77}$$

$$\eta_K^{\text{SD}} = \frac{\left\| (\rho\mathbf{v})_p - (\rho\mathbf{v})_{p-1} \right\|_{L^2(K)}}{\left\| (\rho\mathbf{v})_p \right\|_{L^2(K)}}, \tag{78}$$

where the normalization is given by the volume of the element, $|K|$, and the total energy in the element, $\left\| (\rho\mathbf{v})_p \right\|_{L^2(K)}$, for the SSED and the SD indicators, respectively.

Regarding the marking strategy, initially we had used the local threshold strategy defined by Eq. (68), similarly to Section 5.1. However, this strategy proved to be inadequate when comparing indicators of different nature in the context of the more complex backward-facing step. The reason is that we are dealing with differences of several orders of magnitude between the estimators, especially when comparing the SSED and SD indicators to the multiwavelet-based indicators. Therefore it was not possible to find a user-defined tolerance that fitted them all satisfactorily and kept the comparison meaningful. In a more general framework, it might be more convenient to opt for the maximum marking strategy as defined by Eq. (69), in which the refining threshold is defined as a percentage of the highest value of the indicator. This allows us to set a given fraction of elements to be marked independently of the value of the indicator.

Fig. 13 shows the final adapted grids resulting from applying the h-adaptive algorithm driven by the multiwavelet-based indicators (MW-$\rho\mathbf{v}$, MW-p, and MW-ω) and the two indicators from the literature (SD and SSED). The leftmost column corresponds to the simulation $p = 1$ and its associated initial uniform grid is Mesh C. The column in the middle corresponds to $p = 2$ and the starting grid is Mesh B. Finally, the rightmost column corresponds to the simulation starting from Mesh A and a polynomial degree equal to $p = 3$.

The adapted grids associated with the lowest degree $p = 1$ exhibit the highest number of refined elements. Clearly, the SSED indicator in Fig. 13(e) produces the finest grid. This is due to the fact that it tends to over-refine along the entire channel. However, it only manages to partially capture the geometrical jump. This tendency to over-refining is explained by the low-order approximation used in this simulation. It does not have enough modes to capture the high-frequency content of the solution and thus the indicator, which measures the energy of the highest modes, does not properly work [7]. On the other hand, the SD indicator in Fig. 13(d) is refining aggressively at the walls and along the recirculation bubbles (locations $x = 6h$ and $x = 14h$). This behavior is expected due to its normalization by the total energy of the flow, which approaches zero near walls. This makes the indicator to detect regions that simultaneously report low values of high-frequency content and of the total energy, such as recirculation regions [9]. On the other hand, the refinement produced by the multiwavelet-based indicators is more consistent with the physics, with similar patterns of h-refinement for all indicators. Indeed, the MW-$\rho\mathbf{v}$ and MW-ω indicators, reported in Figs. 13(a) and 13(c), respectively, follow the dynamics of the flow and refine the stream accordingly, with the latter showing a slightly lower number of adapted elements overall. The region around the geometrical jump together with the separated shear layer yields the highest level of refinement. The top and bottom recirculation regions caused by the separation of the flow at the step corner are also adapted to a lesser extent, which can be explained by the regularity of the solution in that region. The MW-p indicator given in Fig. 13(b) displays a higher tendency to refine the region around the step and the separated shear layer. Moreover, it emphasizes adaptation where the flow changes direction to fill the expanded channel (between $x = 6h$ and $x = 14h$), as the pressure changes abruptly in this region.

We now draw our attention to the final adapted grid associated with $p = 3$. We observe that a much lower level of h-refinement is displayed by the adapted grid. This is expected as the grid cell now holds a larger amount of information (corresponding to more DOFs). Yet, regions with geometrical singularities will stand out. Surely, the MW-$\rho\mathbf{v}$ and MW-ω indicators shown in Fig. 13(a) and Fig. 13(c), respectively,

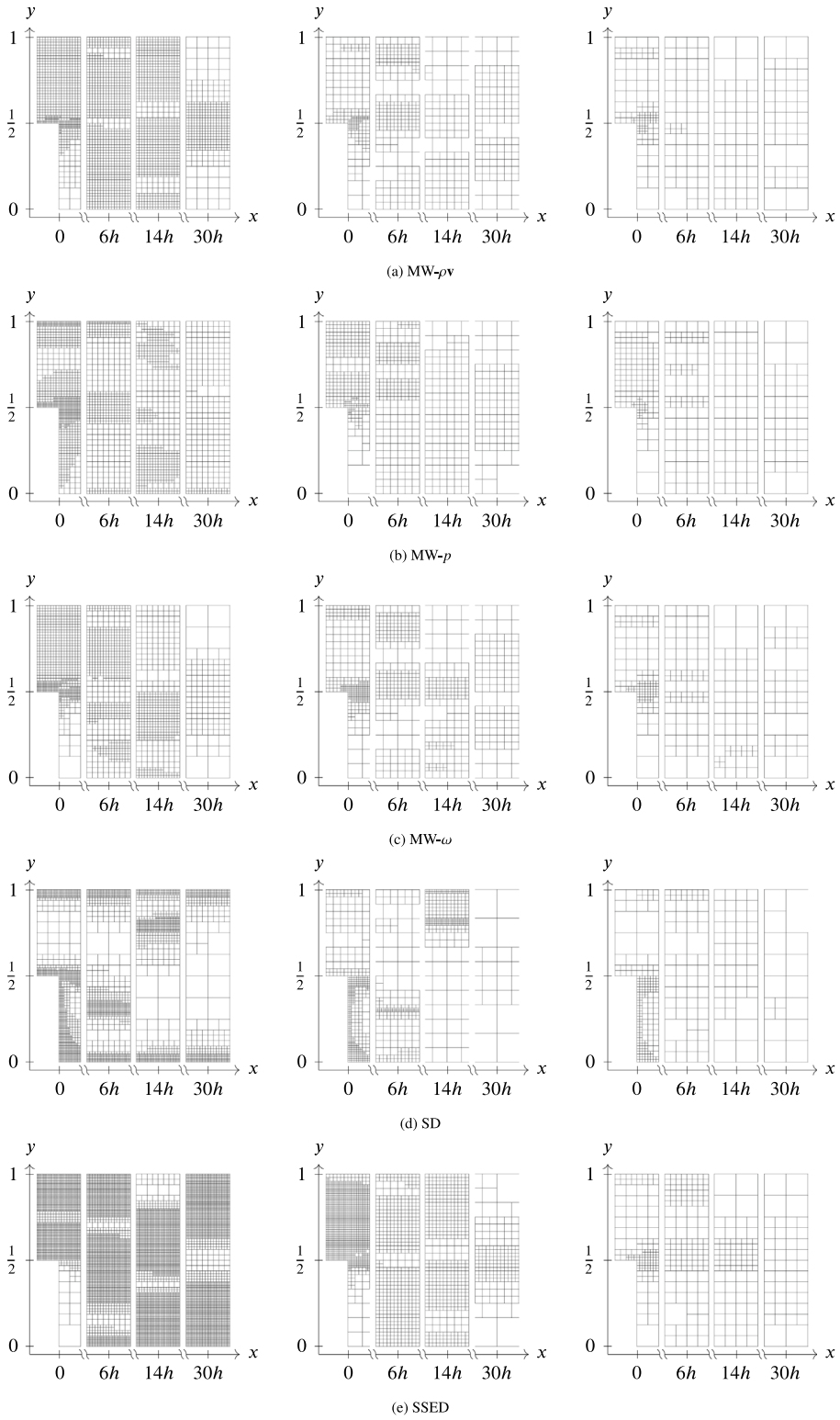

(a) MW-ρv

(b) MW-p

(c) MW-ω

(d) SD

(e) SSED

Fig. 13. Laminar backward-facing-step. Final h-refined grids at four regions along the expanded channel. Figures are organized by error estimator and computational degree, from $p = 1$ (left column), $p = 2$ (middle column), and $p = 3$ (right column).

focus the adaptation efforts on the separated shear layer and in the vicinity of the step. Indeed, a strong velocity gradient appears due to presence of the geometrical jump. In comparison, the lower and upper recirculation regions along the expanded channel undergo little refinement. Similar conclusions can be obtained for the MW-p indicator in Fig. 13(b). The main difference lies in the further refinement along the inlet channel. The higher count of DOFs allows the SSED indicator in Fig. 13(e) to amend the deficiencies reported for the low-order approximation, obtaining a similar pattern of h-refinement as compared to the multiwavelet-based indicators. Though still gaining a larger

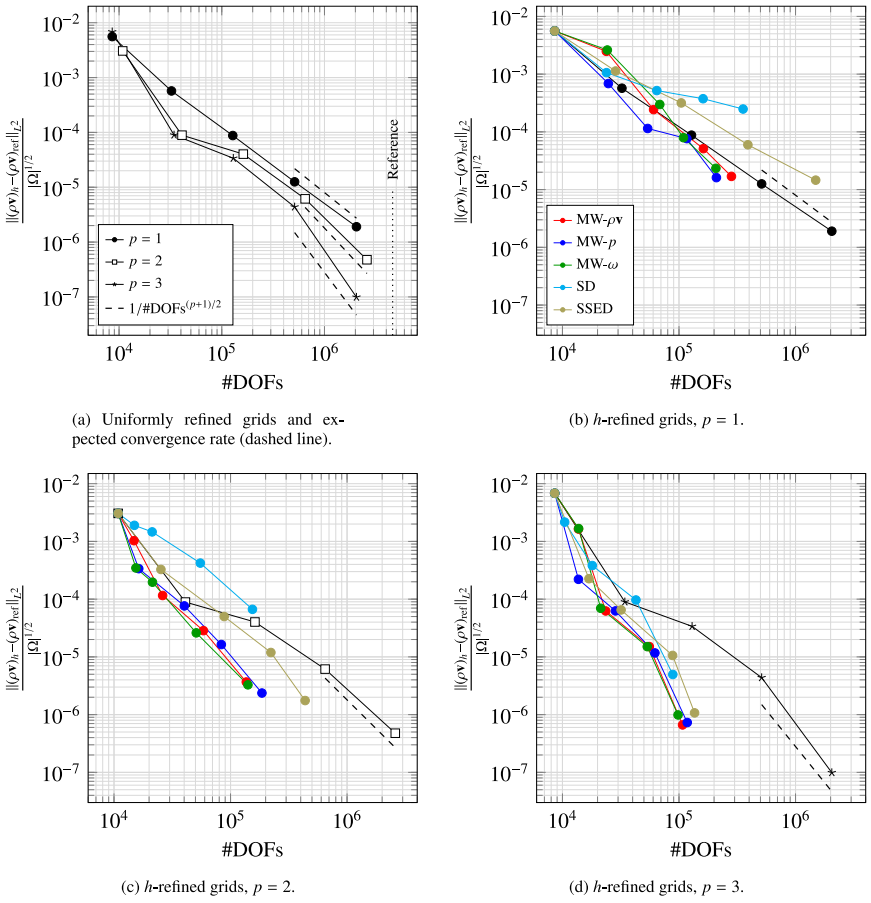

(a) Uniformly refined grids and expected convergence rate (dashed line).

(b) h-refined grids, $p = 1$.

(c) h-refined grids, $p = 2$.

(d) h-refined grids, $p = 3$.

Fig. 14. Laminar backward-facing-step. L^2-norm of the error in momentum density vs the number of degrees of freedom under uniform and adaptive h-refinement for different values of p.

number of elements in general. Fig. 13(d) shows that the SD indicator also benefits from a larger number of DOFs per element. It does fully correct the behavior on the walls but still continues to over-refine in the lower recirculation region.

Lastly, regarding the final adapted grid obtained for the quadratic approximation $p = 2$, it appears to be in between those obtained for $p = 1$ and $p = 3$. Indeed, Figs. 13(a) to 13(c) show how the multiwavelet-based estimators moderately follow the changing stream right after the channel expansion. This behavior is less pronounced for the MW-p indicator in Fig. 13(b), which tends to refine more elements in the inlet region. As for the adaptive $p = 1$ simulation, the multiwavelet estimators lead to the highest level of refinement in the shear layer and in the region in the proximity of the corner, while the more regular recirculation regions display a considerable lower refinement level, closer to the grids obtained for $p = 3$. With respect to the SSED and SD indicators, the increase in the number of DOFs somewhat lessens the deficiencies observed in $p = 1$. Fig. 13(e) shows a more targeted adaptation with the SSED indicator, though still heavily refining along the inlet and immediately after. The SD indicator in Fig. 13(d) significantly reduces refinement closer to walls while excessively adapting the recirculation regions akin to $p = 1$.

In order to measure the accuracy of the h-refined solutions resulting from the different indicators, we will analyze the convergence history of the error in the L^2-norm of the momentum density versus the number of DOFs. To complete the analysis, we will also include an examination of the computational times. Later we will study the locations of flow detachment/reattachment along the expanded channel versus the #DOFs. The reference solution employed to obtain these error quantities is based on the uniform mesh K described in Fig. 11(c) and $p = 2$.

Fig. 14 shows the convergence history of the error in the L^2-norm of the momentum density under uniform and adaptive h-refinement for different orders of the DGM. The evolution of the error on the uniform grids is recorded in Fig. 14(a). We start the adaptation from relatively coarse grids and we want to make sure that we eventually achieve the asymptotic region. Indeed, the plotted data confirm that the asymptotic convergence rate is reached for sufficiently fine grids. The later convergence behavior observed in the higher-order solutions can be explained due to the influence of the singularity at the step.

Figs. 14(b) to 14(d) describe the behavior of the error in the h-adaptive solutions driven by the five error estimators. We make the observation that the maximum local refinement level is limited to reaching the same element size as its uniform counterpart. Aside from the starting grid, four uniformly refined simulations are reported, therefore four refinement steps are performed for each indicator. That explains why the h-refinement procedure does not match the accuracy of the uniform grids. As we previously explained while describing the adapted grids in Fig. 13, the SD and SSED indicators perform poorly for low-orders of the solution. This is due to their dependency on the higher modes of the numerical approximation, which are not well captured for low-orders. By contrast, the multiwavelet-based estimators do not show this dependence and their behavior is more consistent for every order of the adapted solution.

This is evident in Fig. 14(b) with $p = 1$, where the error line of the SD and SSED indicators lies above the uniformly refined line, meaning that no benefit is gained by activating adaptation with these indicators. In the case of the SD indicator the extremely slow decay of the error is explained by its tendency to incorrectly refine on walls and recirculations regions, which are not the main source of error in the backward-facing step configuration. The SSED indicator actually

Table 1
Laminar backward-facing-step. #DOFs and memory comparison for final h-adapted grids. Percentages are measured with respect to uniform grids that report similar solution accuracy. Positive percentages represent savings, while negative values mean higher #DOFs/memory consumption.

Error	#DOFs change (%)			Memory change (%)		
estimator	$p=1$	$p=2$	$p=3$	$p=1$	$p=2$	$p=3$
MW-ρ**v**	30	83	90	33	82	89
MW-p	48	84	88	52	81	87
MW-ω	31	83	89	35	82	89
SD	−491	−120	82	−481	−114	79
SSED	−198	66	84	−220	64	82

Table 2
Laminar backward-facing-step. Memory change for final h-adapted grids. Percentages are evaluated with respect to an equivalent uniform grid with fixed $p=1$. Positive percentages speak for higher memory consumption, while negative values describe a lower memory utilization.

Error estimator	h-refined (%)			Uniform refinement (%)		
	$p=1$	$p=2$	$p=3$	$p=1$	$p=2$	$p=3$
MW-ρ**v**	−33	−56	−53	–	145	320
MW-p	−52	−44	−52	–	204	280
MW-ω	−35	−40	−42	–	238	371
SSED	220	23	−43	–	244	221

manages to reach the same level of accuracy than the multiwavelet-based indicators but at the expense of much larger amount of degrees of freedom, a clear sign of over-refining. On the other hand, the family of multiwavelet-based indicators leads to a moderate reduction of 30% to 48% in the total number of DOFs as compared to uniform refinement, with the MW-p indicator reporting the highest savings.

When the polynomial degree is increased to $p=2$, as illustrated in Fig. 14(c), the multiwavelet-based indicators lead to a reduction of one order of magnitude in the error with respect to $p=1$ while keeping an equivalent total number of degrees of freedom. When they are measured against uniform refinement with the same total error we obtain a decrease of the total number of DOFs of approximately 80%. By contrast, the SSED indicator achieves a similar level of accuracy but reporting a significantly lower performance of about 66%. Its tendency to over-refine is ameliorated but not fully corrected. In a similar manner, the SD indicator seems to slightly improve its behavior compared to $p=1$ but it still retains a slower convergence rate than the uniformly refined simulations and it continues to lag behind the other indicators.

Finally the highest order of the h-adapted solution with $p=3$ is reported in Fig. 14(d). Every error estimator lead to substantial reduction of the required number of degrees of freedom to attain a given level of accuracy. Again, the error is further decreased compared to lower degrees for a similar number of DOFs. The multiwavelet-based indicators achieve the best performance, with savings of approximately 90% compared to uniform refinement. The differences are small, but the MW-ρ**v** indicator reports a small lead. The family of multiwavelet-based indicators become more accurate when we increase the number of DOFs because more information can be efficiently stored by the multiwavelet coefficients. In the same way, a higher-order solution also benefits the SSED and SD indicators. The former achieves a reduction in the total number of DOFs of about 84%, while the latter shows a slightly slower convergence rate only reaching in accuracy the third uniformly refined simulation with savings of around 82%.

Table 1 offers a summary of the savings in the number of degrees of freedom when the h-adaptive algorithm is activated. The multiwavelet-based indicators display a more consistent and reliable behavior with savings increasing from 30% to 40% for $p=1$ to almost 90% for the highest order. By contrast, the SSED and SD indicators underperform the multiwavelet family of indicators for the lower-order simulations, and only manage to achieve savings of about 80% for $p=3$. Finally, similar percentages in memory savings show how the number of DOFs and memory are closely linked. Certainly, the differences between these two quantities are not higher than 10%, even when the order is increased. This happens despite the fact that implicit time integration with higher-order DG methods imposes larger memory requirements [4].

Memory behavior is further studied in Table 2. Only those error estimators which reach a similar level of accuracy are analyzed. We have set the memory consumption of the uniformly refined simulation with $p=1$ as reference to measure the effect of increasing the order in memory growth. We observe a constant decrease in memory of approximately 30% to 50% for the multiwavelet family of indicators, almost independently of the order. Conversely, the uniformly refined simulations report an increase of about three to four times in memory requirements following the increment in order to achieve the same prescribed level of accuracy than its h-adapted counterpart. We remark that the irregular results of the SSED indicator are due to its poorly performance for low-order simulations.

Fig. 15 outlines the behavior of the error versus the computational cost for the different h-adaptive simulations. Interestingly, the rate of convergence in CPU-time for the h-adaptive simulations with $p=1$ is slower in the last iterations than the uniformly refined simulations, as illustrated by Fig. 15(a). We expect this result for the SD and SSED indicators, as they report significantly higher number of degrees of freedom than the uniform simulations for a similar accuracy (see Table 1). However, the multiwavelet estimators do show moderate number of DOFs reductions which do not translate into computational savings. This may occur because for a similar number of DOFs adapted meshes with hanging nodes may take longer to reach convergence than uniform ones.

On the other hand, higher order simulations report clear computational gains when adaptation is activated. This is the case of Fig. 15(b) with $p=2$, where most of the estimators except the SD outperform uniform refinement. This trend continues for $p=3$, with Fig. 15(c) reporting substantial cost improvements for every indicator. Remarkably, the multiwavelet indicators provide the best performance among all the proposed error estimators.

Table 3 collects the CPU-time and speedup values of the h-adaptive simulations applied to the final adapted grids. These quantities are relative to the final uniformly refined mesh. As reported in Fig. 15, we observe a strong variation depending on the order of the adapted solution and the error estimator employed. In this manner, adaptation with $p=1$ underperforms compared to uniform refinement, whereas higher orders achieve significant speedups for selected estimators. The SD indicator offers the lowest performance, with no gain in $p=2$ and a speedup of three times in $p=3$. Conversely, the multiwavelet indicators are the most efficient, delivering more than 20 times faster solutions in $p=2$ and between 12 and 19 times in $p=3$. Lastly, the SSED indicator lands in between, by providing a speedup of five times in $p=2$ and of nine in $p=3$. Sensor estimation, element marking and refining times have not been included in the previous analysis. However, they never constitute more than 5 % of the total computational time.

We complete the study of the adapted solutions by analyzing the normalized lengths of flow separation/reattachment. Unlike the previous analysis of the error, these quantities can be found in literature and thus it will allow us to contrast and validate our results. Table 4 collects some of the most relevant studies and how their values compare to our reference solution. Their domains are slightly different with the main divergence being the length of the expanded channel and the absence/presence of the inlet channel. As reported by Barton [51], the presence of an inlet has resulted in the reduction of the lower reattachment length, denoted by x_1, the upper separation length, x_2, and to a lesser extent, the upper reattachment length, x_3, with respect to the use of no entrance at all. Only the study of Erturk [52] provides results on the separation length at the step, x_0. Our reference solution

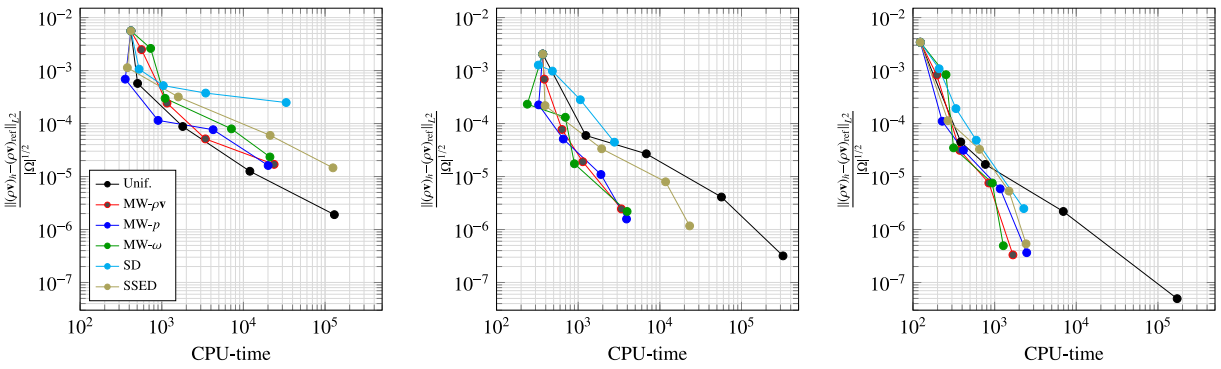

(a) $p = 1$. (b) $p = 2$. (c) $p = 3$.

Fig. 15. Laminar backward-facing-step. L^2-norm of the error in momentum density vs the computational time under uniform and adaptive h-refinement for various values of p.

Table 3
Laminar backward-facing-step. Simulation time speedups between uniform and adapted grids for the final adaptation step in Fig. 15. The results are presented for the different values of p.

(a) $p = 1$.

Indicator	CPU-time (%)	Speedup
Uniform	100.00	1.00
MW-ρ**v**	264.26	0.38
MW-p	223.30	0.45
MW-ω	352.23	0.28
SD	3713.44	0.03
SSED	1250.00	0.08

(b) $p = 2$.

Indicator	CPU-time (%)	Speedup
Uniform	100.00	1.00
MW-ρ**v**	4.22	23.68
MW-p	3.91	25.59
MW-ω	4.41	22.65
SD	100.00	1.00
SSED	21.06	4.75

(c) $p = 3$.

Indicator	CPU-time (%)	Speedup
Uniform	100.00	1.00
MW-ρ**v**	5.23	19.10
MW-p	8.24	12.14
MW-ω	5.56	18.00
SD	32.90	3.05
SSED	11.03	9.07

Table 4
Laminar backward-facing-step. Normalized separation and reattachment locations found in literature.

	x_0	x_1	x_2	x_3	Domain
Gartling [54]	–	12.20	9.70	20.96	$60h$, no entrance
Barton [51]	–	12.03	9.64	20.96	$32h$, no entrance
	–	11.51	9.14	20.66	$32h$ + inlet channel ($10h$)
Cruchaga [56]	–	12.00	9.60	20.20	$60h$, no entrance
	–	12.00	9.40	19.40	$60h$ + inlet channel (h)
Erturk [52]	0.15	11.83	9.47	20.55	$300h$ + inlet channel ($20h$)
Present study	0.15	11.81	9.31	20.83	$60h$ + inlet channel ($5h$)

agrees very well with the values x_0 and x_1 provided by Erturk. The lengths x_2 and x_3, defining the upper recirculation region, show a small deviation from the study. However, the former is still within the values provided by Cruchaga [56] and Barton [51], and the latter, being the furthest from the step, is the least influenced by the absence/presence of the inlet channel and thus it is reasonable that it may be found to be in between the estimates given by Barton.

Fig. 16 shows the convergence history of the normalized separation/reattachment lengths for every error estimator and different orders of the numerical solution. The evolution of the separation length at the step, denoted by x_0, shines a new light on indicator behavior not reported in the previous analysis of Fig. 14. Certainly, the SD indicator shows the fastest convergence and highest accuracy of the error estimators examined. Moreover, it is the only indicator that reaches the target reference length when $p > 1$ while achieving a large reduction on the number of degrees of freedom (above 90%) compared to uniform refinement. This unusual result can be explained by two confluent factors. These are, the weak influence of the stream itself on this region and the strong tendency of the SD indicator to refine in the low energy regions. The first factor ameliorates the poor performance of the indicator overall, and the second factor allows for over-refining in the recirculation regions, which is beneficial to accurately secure the separation/reattachment locations. By contrast, the rest of the indicators do not focus as much on regions of low energy and thus struggle to reach the target length.

The convergence history of the remaining locations x_1, x_2, and x_3 shows patterns already observed during the previous analysis of the error in Fig. 14. For the lowest degree $p = 1$, the SD indicator reports the largest divergence on achieving the reference target length. This happens despite its tendency to heavily refine in recirculation regions and on walls, which should help convergence to the target length. This contradiction can be explained by the higher weight that the upstream flow acquire on accurately capturing the locations further from the step. Therefore, efficient refinement in of the upstream flow is key. On the other hand, the SSED indicator displays mixed record on reaching the reference target length, together with a slower convergence rate compared to uniform refinement. Finally, the multiwavelet-based indicators show analogous rates of convergence between them when analyzing x_1, x_2, and x_3 for $p = 1$ simulations. Apart from x_3, for which only the MW-ρ**v** indicator achieves the target, every multiwavelet-based estimator reaches the reference value with savings in the range of 45% to 60%.

When the order is increased to $p = 2$, every indicator substantially improves their convergence rate. The SSED indicator attains a reduction of about 83% in the number of DOFs and the multiwavelet-based indicators obtain a further decrease to be within the interval of 93% to 95%. The SD indicator remains as the only error estimator which does not achieve the target length.

Finally, for the highest order $p = 3$ every refinement indicator reaches the prescribed reference length while achieving a significant reduction in the number of DOFs. They perform similarly within the savings range of 93% to 96%. The exception is the upper reattachment length, x_3, for which the MW-ω and the SSED indicators do not converge to the target. It is also worth mentioning that in this case the SD indicator performs better than in previous Fig. 14, due to the idiosyncrasy of the separation/reattachment location quantity, which generally will show better measurements from indicators that lean toward refinement on the recirculation regions.

To finalize our work, we examine the different indicators within the multiwavelet family. So far, when comparing them to the SSED and SD indicators we have treated them mainly as a group. Now we analyze their performance with respect to each other. To do that, we evaluate the error in the L^2-norm of the different physical quantities that characterize each of the multiwavelet indicators along vertical profiles at the

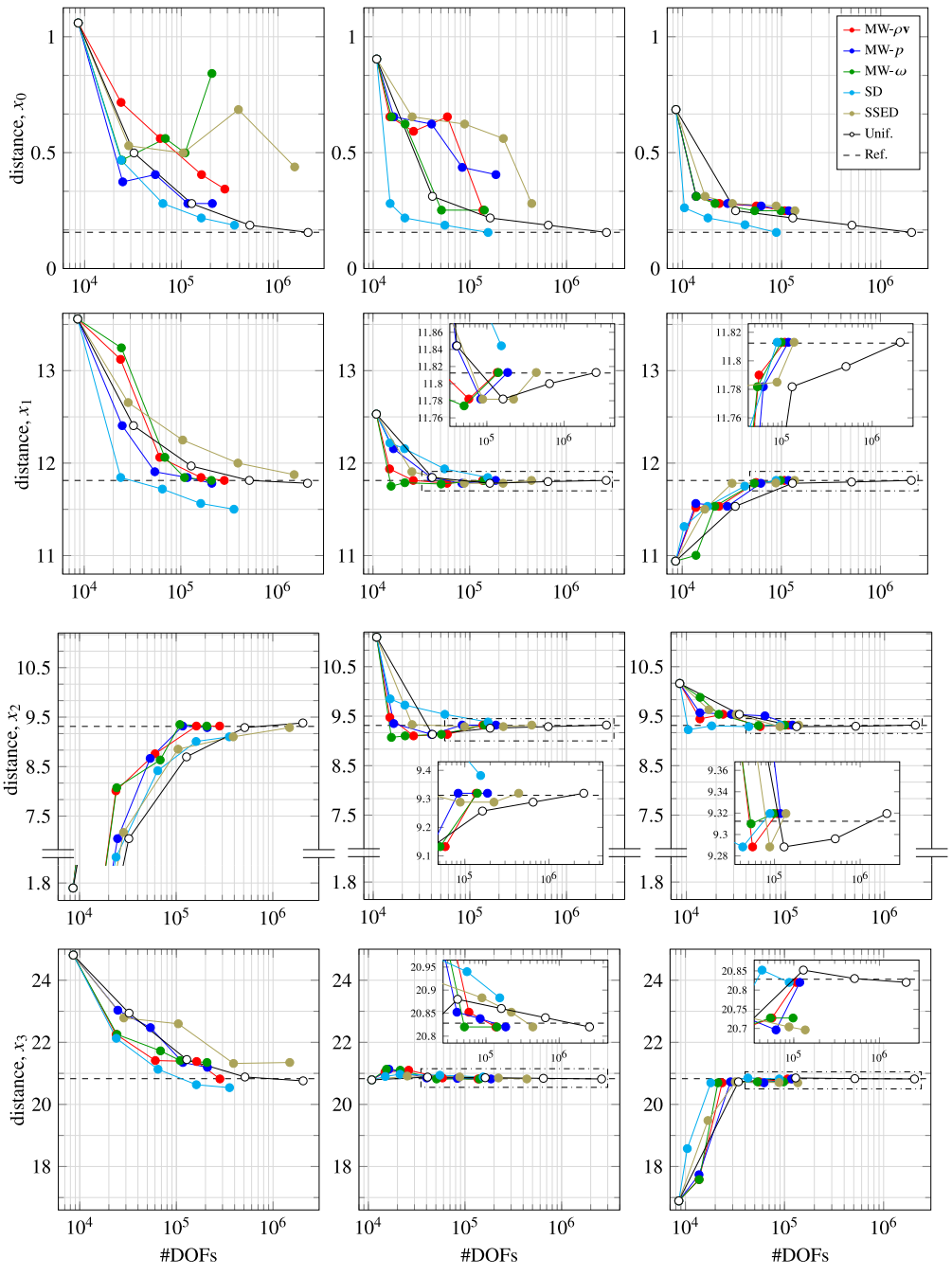

(a) $p = 1$. **(b)** $p = 2$. **(c)** $p = 3$.

Fig. 16. Laminar backward-facing-step. Normalized locations of flow detachment/reattachment under uniform and adaptive h-refinement for varying values of p.

selected locations $x = 0, 6h, 14h, 30h$ shown in Fig. 11(a). We remind the reader that the indicators encompass density momentum, pressure and vorticity, and thus the error is based on these as well. We assume that the final adapted grid reaches an equivalent level of accuracy for every indicator of the multiwavelet family, as reported in Fig. 14 for the density momentum, so that we have a meaningful comparison.

Fig. 17 shows the comparison between the multiwavelet-based indicators. Figs. 17(b) and 17(d) represent every profile location along the x-axis and its associated error along the y-axis. For each figure there are three line styles covering $p = 1$ to $p = 3$. Color preference is given to those indicators that typify the same physical quantity than the current error. For example, Fig. 17(b) illustrates the error in momentum density, and thus the red color line represents the h-adapted mesh associated to the momentum density indicator, MW-ρ**v**. The remaining black lines represent the h-adapted mesh driven by the pressure indicator, MW-p, and vorticity indicator, MW-ω, in no preferential order. In general, we observe that $p = 1$ reports a more even distribution of error along the channel. When we increase the approximation order the error is concentrated in the region around the step while decreasing at the other locations, a clear sign that the downstream convection of the error is ameliorated. Interestingly, the best results in these locations $x > 0$ with $p > 1$ are generally obtained by the indicator that share physical variable with the error, e.g. error in pressure is better captured by the MW-p indicator. This is somehow expected, as an indicator based on a particular physical variable would usually monitor better its associated error.

Fig. 17(a) measures the error of these profiles combined. We observe that for low-order and evenly distribution of the error, the MW-ρ**v**

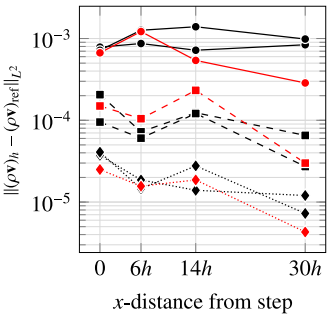

(a) L^2-norm of the error in momentum density.

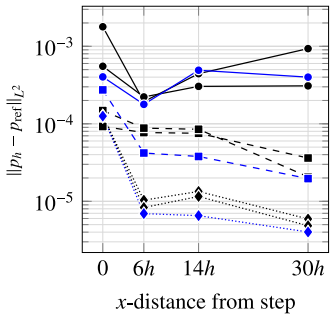

(b) L^2-norm of the error in pressure.

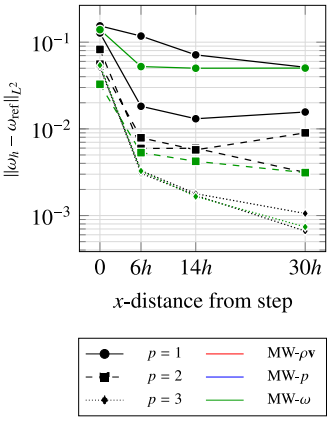

(c) L^2-norm of the error in vorticity.

Error estimator	$p = 1$	$p = 2$	$p = 3$
	$\|(\rho\mathbf{v})_h - (\rho\mathbf{v})_{\text{ref}}\|_{L^2}$		
MW-$\rho\mathbf{v}$	1.52×10^{-3}	2.97×10^{-4}	3.51×10^{-5}
MW-p	1.61×10^{-3}	2.59×10^{-4}	4.56×10^{-5}
MW-ω	2.24×10^{-3}	1.68×10^{-4}	5.19×10^{-5}
	$\|p_h - p_{\text{ref}}\|_{L^2}$		
MW-$\rho\mathbf{v}$	7.36×10^{-4}	1.93×10^{-4}	1.26×10^{-4}
MW-p	7.71×10^{-4}	2.80×10^{-4}	1.26×10^{-4}
MW-ω	2.07×10^{-3}	1.47×10^{-4}	1.27×10^{-4}
	$\|\omega_h - \omega_{\text{ref}}\|_{L^2}$		
MW-$\rho\mathbf{v}$	1.31×10^{-1}	8.30×10^{-2}	5.33×10^{-2}
MW-p	2.13×10^{-1}	5.73×10^{-2}	5.08×10^{-2}
MW-ω	1.65×10^{-1}	3.35×10^{-2}	5.43×10^{-2}

(d) L^2-norm of the total error (combined profiles). Best result given by cell in grey.

Fig. 17. Laminar backward-facing step. Performance comparison with varying p among multiwavelet-based error estimators at selected profiles along the expanded channel..

indicator offers the best performance, reporting the most accurate results in momentum density, pressure, and vorticity. When the order is increased, the step region gains more influence and the indicator that reports lower error there will perform best. In our case it is the MW-ω indicator for $p = 2$ and a combination of the MW-$\rho\mathbf{v}$ and MW-p for $p = 3$. Therefore, we believe that near a singularity there is no clear indicator that outperform the others. All of them perform similarly, with slight variations depending on the order of the simulation.

6. Conclusions

In this work we have presented a family of novel error estimators to perform h-adaptation based on a local multiwavelet analysis of the DG solution of conservation laws. This high-order solution is subjected to a post-enrichment process so that the multiwavelet expansion is able to extract meaningful information from the locally enriched DG solution. The new information is represented in the form of multiwavelet coefficients, on which is based the computation of the error estimators.

First simulations of the one-dimensional viscous Burgers equation show convincing results. For these simulations an important decrease in the number of degrees of freedom is observed when the adaptive process is activated. A comparison of the performance of the proposed approach with the modal error estimators developed in [7,8] shows that, for our proposed indicators, fewer elements are refined for a given error level. Interestingly, the effectivity index of the proposed method is close to unity, which means that it is able to closely monitor the evolution of the error in the approximation.

Supported by the encouraging results of the one-dimensional simulations, we have extended the multiwavelet-based error estimators to higher dimensions. The 2-D approach is applied to a steady laminar backward-facing step flow at $Re = 800$ and $Ma = 0.1$. This more challenging configuration certainly demonstrates the viability of h-refinement to reach a substantial computational gain with respect to uniformly refined grids. For a prescribed level of accuracy, depending on the order of the simulation, the multiwavelet-based indicators have achieved a reduction in the numbers of degrees of freedom of 48%, 84%, 90% for DG $p = 1$, $p = 2$, and $p = 3$ simulations, respectively. The convergence study of the separation/reattachment lengths leads to similar savings and further justifies the use of h-adaptation to reduce the computational load.

It is worth mentioning that the number of DOFs in the final adapted grid is kept relatively constant for every simulation order. Therefore, the increase in savings is due to the gain in accuracy from the use of higher-order. Most importantly, this improved accuracy with increasing order is achieved while the memory consumption of the h-adaptive simulations remains stable. By contrast, the same methodology applied to uniformly refined simulations leads to an increase of up to four times in memory requirements with respect to adapted simulations. This result highlights the importance of high-order methods in adaptation.

A thorough comparison of the multiwavelet-based indicators versus selected indicators provided by Naddei et al. [7,8] has found the largest differences in behavior for the low-order simulations. Regarding the literature estimators, the SSED indicator performs poorly due to their dependency on the higher modes of the solution, while the underperforming behavior of the SD indicator is due to its tendency to wrongly detect regions in which high-energy content and the total energy have low values. On the other hand, the multiwavelet-based indicators do not show this dependency across the different orders. Most notably, the multiwavelet-based indicators become more accurate when increasing the number of DOFs per element thanks to the higher quantity of details captured during the multiwavelet decomposition. In a similar manner, the SSED and SD indicators also benefit from a larger number of DOFs, which allows for a better representation of higher modes. This is especially relevant for the SSED indicator. However, they still do not surpass the overall performance of the multiwavelet-based indicators.

These differences are highlighted in the analysis of the h-adapted grids. For low-order simulations, the SSED indicator normally produces the largest refined grid, whereas the SD indicator tends to refine aggressively at the walls and along the recirculation regions. By contrast, the multiwavelet-based indicators display a more consistent adaptation, with less dependency on the numerical order. They focus the adaptation efforts on the separated shear layer and on the vicinity of the singularity. These regions display the highest h-refinement levels regardless of p, due to the presence of a sharp velocity gradient. With the exception of the SD indicator, all indicators tend to produce similar patterns of h-refinement as the order is increased. In this case, the multiwavelet-based indicators and the SSED indicator lead to similar refined regions, though the latter still yields a slightly larger mesh.

The size of the mesh and the order of the approximation become key drivers of the magnitude of the simulation times. Computational times need to be interpreted with caution because they are hard to measure consistently and are subjected to many variables not always fully understood. However, the data presented demonstrates that, by activating a multiwavelet-guided adaptation in simulations of higher order, we achieve substantial speedup times. Particularly, in the best case scenario, the multiwavelet indicators enable more than 20 times faster solutions when compared to the non-adapted solution.

With regards to the individual indicators under the umbrella of the multiwavelet philosophy, we have found that, when the underlying solution is smooth and for a prescribed level of accuracy, building the indicator on a physical quantity (e.g. momentum density) leads to h-adapted meshes that report more accurate quantity values than the homologous h-adapted meshes from the remaining multiwavelet-based indicators. However, in the presence of a singularity, the causality seems to be weakened and the choice of the physical quantity for the MW-based indicator seems not to matter as much.

The extension to isotropic hp-adaptation by monitoring the rate of decay of the multiwavelets' vanishing moments is the subject of current research. Future research is also planned on the analysis of the multiwavelet components in the x-, y- and xy- directions, which will open the door to the development of an anisotropic adaptation algorithm.

CRediT authorship contribution statement

Javier García Bautista: Conceptualization, Methodology, Software, Formal analysis, Investigation, Writing – original draft, Visualization. **Marta de la Llave Plata:** Conceptualization, Writing – review & editing, Supervision, Funding acquisition. **Vincent Couaillier:** Writing – review & editing, Supervision, Project administration, Funding acquisition. **Michel Visonneau:** Writing – review & editing, Supervision, Project administration, Resources. **Kai Schneider:** Conceptualization, Formal analysis, Writing – review & editing, Supervision.

Declaration of competing interest

The authors declare that they have no known competing financial interests or personal relationships that could have appeared to influence the work reported in this paper.

Data availability

The authors do not have permission to share data.

Acknowledgments

This project has received funding from the European Union's Horizon 2020 research and innovation program under the Marie Skłodowska-Curie grant agreement No. 675008 for the years 2017 to 2019 and from ONERA for 2020 onwards.

Appendix. Viscous Burgers Equation

In this case $\Omega \subset \mathbb{R}$ and the vector of conservative variables in Eqs. (1)–(2) simply becomes $\mathbf{u} = u$. The convective and viscous fluxes take the form $\mathcal{F}_c(u) = \frac{1}{2}u^2$ and $\mathcal{F}_v\left(u, \partial_x u\right) = \nu \frac{\partial u}{\partial x}$, respectively. Finally, the variational projection of the convective and viscous terms in Eq. (4) yields

$$\mathcal{L}_c(u_h, \phi_h) = \left[h_c \phi_h\right]_{\partial K} - \int_K \tfrac{1}{2} u_h^2 \frac{\partial \phi_h}{\partial x}\,\mathrm{d}x\,, \tag{A.1}$$

$$\mathcal{L}_v(u_h, \phi_h) = -\nu \left(\left[\Theta_v \phi_h\right]_{\partial K} - \int_K \frac{\partial u_h}{\partial x}\frac{\partial \phi_h}{\partial x}\,\mathrm{d}x - \left[(h_v - u_h)\frac{\partial \phi_h}{\partial x}\right]_{\partial K} \right), \tag{A.2}$$

in which the structure presented by Alhawwary and Wang [57] has been followed. Similarly to the 2-D formulation reported in Section 2.1, the LLF flux is employed. Therefore:

$$h_c = \left\{\!\!\left\{ \mathcal{F}_c(u) \right\}\!\!\right\} - \frac{1}{2}\alpha^{\mathrm{LLF}} [\![u]\!]\,, \tag{A.3}$$

with

$$\alpha^{\mathrm{LLF}} = \max_{\min(u^-,u^+)\le u \le \max(u^-,u^+)} \left| \frac{\mathrm{d}\mathcal{F}_c(u)}{\mathrm{d}u} \right|\,. \tag{A.4}$$

The numerical viscous fluxes, h_v and Θ_v, are approximated by the symmetric interior penalty method described by Arnold et al. [58]. It reads

$$h_v = \left\{\!\!\left\{ u_h \right\}\!\!\right\}\,, \tag{A.5}$$

$$\Theta_v = \left\{\!\!\left\{ \frac{\partial u_h}{\partial x} \right\}\!\!\right\} - \alpha^{\mathrm{SIP}} [\![u_h]\!]\,. \tag{A.6}$$

The penalty parameter, α^{SIP}, depends on the size of the element and the polynomial degree p [57].

For the time integration an explicit time marching scheme is employed, the strong stability preserving (SSP) 3rd-order 4-stage Runge–Kutta method [59]. Consequently, Eq. (4) can be expressed as

$$M_K^{\ell\ell} \frac{\partial U_K^\ell}{\partial t} = \mathcal{L}_K^\ell \left(U_{K-1}^\ell, U_K^\ell, U_{K+1}^\ell\right), \tag{A.7}$$

where

$$M_K^{\ell\ell} = \int_K \phi_K^\ell \phi_K^\ell \mathrm{d}x\,, \qquad \forall K \in \Omega_h\,. \tag{A.8}$$

The term $\mathcal{L}_K^\ell \left(U_{K-1}^\ell, U_K^\ell, U_{K+1}^\ell\right)$ encompasses the convective and viscous terms of Eqs. (A.1)–(A.3), and the DOFs are the unknowns of the system of ordinary differential equations.

References

[1] García Bautista J, de la Llave Plata M, Couaillier V, Visonneau M, Schneider K. Local multiwavelet-based adaptation within a discontinuous Galerkin framework. In: AIAA Scitech 2021 Forum. 2021, http://dx.doi.org/10.2514/6.2021-1780.

[2] Chapelier J-B, de la Llave Plata M, Renac F, Lamballais E. Evaluation of a high-order discontinuous Galerkin method for the DNS of turbulent flows. Comput & Fluids 2014;95:210–26. http://dx.doi.org/10.1016/j.compfluid.2014.02.015.

[3] Chapelier J-B, de la Llave Plata M, Renac F. Inviscid and viscous simulations of the Taylor-green vortex flow using a modal discontinuous galerkin approach. In: 42nd AIAA fluid dynamics conference and exhibit. 2012, http://dx.doi.org/10.2514/6.2012-3073.

[4] Renac F, de la Llave Plata M, Martin E, Chapelier JB, Couaillier V. Aghora: A high-order DG solver for turbulent flow simulations. In: IDIHOM, Vol. 1. Springer International Publishing; 2015, p. 315–35. http://dx.doi.org/10.1007/978-3-319-12886-3_15.

[5] Ferziger J, Perić M, Street R. Computational methods for fluid dynamics. 4th ed.. Springer International Publishing; 2020, http://dx.doi.org/10.1007/978-3-319-99693-6.

[6] LeVeque RJ. Finite volume methods for hyperbolic problems. Cambridge University Press; 2002, http://dx.doi.org/10.1017/CBO9780511791253.

[7] Naddei F, de la Llave Plata M, Couaillier V. A comparison of refinement indicators for *p*-adaptive discontinuous galerkin methods for the euler and navier-stokes equations. 2018 AIAA Aerospace Sciences Meeting; 2018, http://dx.doi.org/10.2514/6.2018-0368.

[8] Naddei F, de la Llave Plata M, Couaillier V, Coquel F. A comparison of refinement indicators for *p*-adaptive simulations of steady and unsteady flows using discontinuous Galerkin methods. J Comput Phys 2019;376:508–33. http://dx.doi.org/10.1016/j.jcp.2018.09.045.

[9] Naddei F. Simulation adaptative des grandes échelles d'écoulements turbulents fondée sur une méthode galerkine discontinue [Ph.D. thesis], (2019SACLX060). Université Paris Saclay (COmUE); 2019.

[10] Mallat S. A wavelet tour of signal processing. 3rd ed.. Academic Press Inc.; 2008, http://dx.doi.org/10.1016/B978-0-12-374370-1.X0001-8.

[11] Strela V. Multiwavelets–theory and applications [Ph.D. thesis], Massachusetts Institute of Technology; 1996.

[12] Harten A. Multiresolution representation of data: A general framework. SIAM J Numer Anal 1996;33(3):1205–56. http://dx.doi.org/10.1137/0733060.

[13] Müller S. Adaptive multiscale schemes for conservation laws, Vol. 27. Springer-Verlag Berlin Heidelberg; 2003, http://dx.doi.org/10.1007/978-3-642-18164-1.

[14] Müller S. Multiresolution schemes for conservation laws, Vol. 1. Springer-Verlag Berlin Heidelberg; 2009, p. 379–408. http://dx.doi.org/10.1007/978-3-642-03413-8_11.

[15] Roussel O, Schneider K, Tsigulin A, Bockhorn H. A conservative fully adaptive multiresolution algorithm for parabolic PDEs. J Comput Phys 2003;188(2):493–523. http://dx.doi.org/10.1016/S0021-9991(03)00189-X.

[16] Domingues MO, Gomes SM, Roussel O, Schneider K. Space-time adaptive multiresolution methods for hyperbolic conservation laws: Applications to compressible Euler equations. Appl Numer Math 2009;59(9):2303–21. http://dx.doi.org/10.1016/j.apnum.2008.12.018.

[17] Deiterding R, Domingues MO, Gomes SM, Roussel O, Schneider K. Adaptive multiresolution or adaptive mesh refinement? A case study for 2D Euler equations. In: ESAIM: proc., Vol. 29. 2009, p. 28–42. http://dx.doi.org/10.1051/proc/2009053.

[18] Deiterding R, Domingues MO, Gomes SM, Schneider K. Comparison of adaptive multiresolution and adaptive mesh refinement applied to simulations of the compressible Euler equations. SIAM J Sci Comput 2016;38(5):173–93. http://dx.doi.org/10.1137/15M1026043.

[19] Hovhannisyan N, Müller S, Schäfer R. Adaptive multiresolution discontinuous Galerkin schemes for conservation laws. Math Comp 2014;83(285):113–51. http://dx.doi.org/10.1090/S0025-5718-2013-02732-9.

[20] Gerhard N, Iacono F, May G, Müller S, Schäfer R. A high-order discontinuous Galerkin discretization with multiwavelet-based grid adaptation for compressible flows. J Sci Comput 2015;62(1):25–52. http://dx.doi.org/10.1007/s10915-014-9846-9.

[21] Gerhard N, Caviedes-Voullième D, Müller S, Kesserwani G. Multiwavelet-based grid adaptation with discontinuous Galerkin schemes for shallow water equations. J Comput Phys 2015;301:265–88.

[22] Gerhard N, Müller S. Adaptive multiresolution discontinuous Galerkin schemes for conservation laws: Multi-dimensional case. Comput Appl Math 2016;35:321–49. http://dx.doi.org/10.1007/s40314-014-0134-y.

[23] Gerhard N. An adaptive multiresolution discontinuous Galerkin scheme for conservation laws [Ph.D. thesis], RWTH Aachen University; 2017.

[24] Shelton AB. A multi-resolution discontinuous Galerkin method for unsteady compressible flows [Ph.D. thesis], Georgia Tech; 2008.

[25] Archibald R, Fann G, Shelton W. Adaptive discontinuous Galerkin methods in multiwavelets bases. Appl Numer Math 2011;61(7):879–90. http://dx.doi.org/10.1016/j.apnum.2011.02.005.

[26] Vuik MJ, Ryan JK. Multiwavelet troubled-cell indicator for discontinuity detection of discontinuous Galerkin schemes. J Comput Phys 2014;270:138–60. http://dx.doi.org/10.1016/j.jcp.2014.03.047.

[27] Vuik MJ, Ryan JK. Automated parameters for troubled-cell indicators using outlier detection. SIAM J Sci Comput 2016;38(1):84–104. http://dx.doi.org/10.1137/15M1018393.

[28] Vuik MJ. Multiwavelets and outlier detection for troubled-cell indication in discontinuous Galerkin methods [Ph.D. thesis], Delft University of Technology; 2017.

[29] Alpert BK. A class of bases in L^2 for the sparse representation of integral operators. SIAM J Math Anal 1993;24(1):246–62. http://dx.doi.org/10.1137/0524016.

[30] Alpert B, Beylkin G, Gines D, Vozovoi L. Adaptive solution of partial differential equations in multiwavelet bases. J Comput Phys 2002;182(1):149–90. http://dx.doi.org/10.1006/jcph.2002.7160.

[31] Yu T, Kolarov K, Lynch W. Barysymmetric multiwavelets on triangle. IRC report 1997-006, Standford University; 1999.

[32] Dolejší V, Solin P. hp-discontinuous Galerkin method based on local higher order reconstruction. Appl Math Comput 2016;279:219–35. http://dx.doi.org/10.1016/j.amc.2016.01.024.

[33] Cockburn B. An introduction to the discontinuous galerkin method for convection-dominated problems, Vol. 1. Springer Berlin Heidelberg; 1998, p. 150–268. http://dx.doi.org/10.1007/BFb0096353.

[34] Bassi F, Rebay S. A high-order accurate discontinuous finite element method for the numerical solution of the compressible Navier–Stokes equations. J Comput Phys 1997;131(2):267–79. http://dx.doi.org/10.1006/jcph.1996.5572.

[35] Geronimo JS, Iliev P, Assche WV. Alpert multiwavelets and Legendre-Angelesco multiple orthogonal polynomials. SIAM J Math Anal 2017;49:626–45. http://dx.doi.org/10.1137/16M1064465.

[36] Mavriplis C. Adaptive mesh strategies for the spectral element method. Comput Methods Appl Mech Engrg 1994;116(1):77–86. http://dx.doi.org/10.1016/S0045-7825(94)80010-3.

[37] Mitchell WF, McClain MA. A comparison of hp-adaptive strategies for elliptic partial differential equations. ACM Trans Math Software 2014;41(1). http://dx.doi.org/10.1145/2629459.

[38] Bey KS, Tinsley Oden J. *hp*-Version discontinuous Galerkin methods for hyperbolic conservation laws. Comput Methods Appl Mech Engrg 1996;133(3):259–86. http://dx.doi.org/10.1016/0045-7825(95)00944-2.

[39] Adjerid S, Devine KD, Flaherty JE, Krivodonova L. A posteriori error estimation for discontinuous Galerkin solutions of hyperbolic problems. Comput Methods Appl Mech Engrg 2002;191(11):1097–112. http://dx.doi.org/10.1016/S0045-7825(01)00318-8.

[40] Oden J, Demkowicz L, Rachowicz W, Westermann T. Toward a universal h-p adaptive finite element strategy, part 2. a posteriori error estimation. Comput Methods Appl Mech Engrg 1989;77(1):113–80. http://dx.doi.org/10.1016/0045-7825(89)90130-8.

[41] Rueda-Ramírez AM, Manzanero J, Ferrer E, Rubio G, Valero E. A *p*-multigrid strategy with anisotropic *p*-adaptation based on truncation errors for high-order discontinuous Galerkin methods. J Comput Phys 2019;378:209–33. http://dx.doi.org/10.1016/j.jcp.2018.11.009.

[42] Babuvška I, Rheinboldt W. Error estimates for adaptive finite element computations. SIAM J Numer Anal 1978;15:736–54. http://dx.doi.org/10.1137/0715049.

[43] Dörfler W, Heuveline V. Convergence of an adaptive *hp* finite element strategy in one space dimension. Appl Numer Math 2007;57(10):1108–24. http://dx.doi.org/10.1016/j.apnum.2006.10.003.

[44] Demkowicz L, Oden J, Rachowicz W, Hardy O. Toward a universal h-p adaptive finite element strategy, part 1. constrained approximation and data structure. Comput Methods Appl Mech Engrg 1989;77(1):79–112. http://dx.doi.org/10.1016/0045-7825(89)90129-1.

[45] Bank R, Sherman A. Some refinement algorithms and data structures for regular local mesh refinement. Applications of Mathematics and Computing to the Physical Sciences; 1999.

[46] Berger MJ, Oliger J. Adaptive mesh refinement for hyperbolic partial differential equations. J Comput Phys 1984;53(3):484–512. http://dx.doi.org/10.1016/0021-9991(84)90073-1.

[47] Kuru G, de la Llave Plata M, Couaillier V, Abgrall R, Coquel F. An adaptive variational multiscale discontinuous Galerkin method for large eddy simulation. In: 54th AIAA aerospace sciences meeting. 2016, http://dx.doi.org/10.2514/6.2016-0584.

[48] Taube A, Gassner G, Munz C-D. hp-adaptation in space-time within an explicit discontinuous galerkin framework. Berlin, Heidelberg: Springer Berlin Heidelberg; 2010, p. 427–39. http://dx.doi.org/10.1007/978-3-642-03707-8_30.

[49] Babuvška I, Rheinboldt WC. Reliable error estimation and mesh adaptation for the finite element method. Comput Methods Nonlinear Mech 1980;67–108.

[50] Johnson C. Adaptive finite element methods for diffusion and convection problems. Comput Methods Appl Mech Engrg 1990;82(1):301–22. http://dx.doi.org/10.1016/0045-7825(90)90169-M.

[51] Barton IE. The entrance effect of Laminar flow over a backward-facing step geometry. Internat J Numer Methods Fluids 1997;25(6):633–44. http://dx.doi.org/10.1002/(SICI)1097-0363(19970930)25:6<633::AID-FLD551>3.0.CO;2-H.

[52] Erturk E. Numerical solutions of 2-D steady incompressible flow over a backward-facing step, part I: High Reynolds number solutions. Comput & Fluids 2008;37(6):633–55. http://dx.doi.org/10.1016/j.compfluid.2007.09.003.

[53] Keskar J, Lyn D. Computations of a Laminar backward-facing step flow at *Re*=800 with a spectral domain decomposition method. Internat J Numer Methods Fluids 1999;29(4):411–27. http://dx.doi.org/10.1002/(SICI)1097-0363(19990228)29:4<411::AID-FLD794>3.0.CO;2-6.

[54] Gartling DK. A test problem for outflow boundary conditions—flow over a backward-facing step. Internat J Numer Methods Fluids 1990;11(7):953–67. http://dx.doi.org/10.1002/fld.1650110704.

[55] Yee H, Torczynski J, Morton S, Visbal M, Sweby P. On spurious behavior of CFD simulations. In: 13th computational fluid dynamics conference. 1997, http://dx.doi.org/10.2514/6.1997-1869.

[56] Cruchaga MA. A study of the backward-facing step problem using a generalized streamline formulation. Commun Numer Methods Eng 1998;14(8):697–708. http://dx.doi.org/10.1002/(SICI)1099-0887(199808)14:8<697::AID-CNM155>3.0.CO;2-0.

[57] Alhawwary M, Wang ZJ. On the accuracy and stability of various DG formulations for diffusion. In: Numerical analysis. 2018, arXiv.

[58] Arnold DN, Brezzi F, Cockburn B, Marini LD. Unified analysis of discontinuous Galerkin methods for elliptic problems. SIAM J Numer Anal 2002;39(5):1749–79. http://dx.doi.org/10.1137/S0036142901384162.

[59] Carpenter MH, Kennedy CA. Fourth-order 2N-storage Runge-Kutta schemes. NASA reports TM, 109112, 1994.